The carbonate pump feedback on alkalinity and the carbon cycle in the 21st century and beyond

Alban Planchat, Laurent Bopp, Lester Kwiatkowski, Olivier Torres

Earth System
Dynamics

The carbonate pump feedback on alkalinity and the carbon cycle in the 21st century and beyond

Alban Planchat[1], Laurent Bopp[1], Lester Kwiatkowski[2], and Olivier Torres[1]

[1]LMD-IPSL, CNRS, École Normale Supérieure/PSL Res. Univ., École Polytechnique,
Sorbonne Université, 75005 Paris, France
[2]LOCEAN Laboratory, Sorbonne Université-CNRS-IRD-MNHN, 75005 Paris, France

Correspondence: Alban Planchat (alban.planchat@lmd.ipsl.fr)

Abstract. Ocean acidification is likely to impact all stages of the ocean carbonate pump, i.e. the production, export, dissolution and burial of biogenic $CaCO_3$. However, the associated feedback on anthropogenic carbon uptake and ocean acidification has received little attention. It has previously been shown that Earth system model (ESM) carbonate pump parameterizations can affect and drive biases in the representation of ocean alkalinity, which is critical to the uptake of atmospheric carbon and provides buffering capacity towards associated acidification. In the sixth phase of the Coupled Model Intercomparison Project (CMIP6), we show divergent responses of $CaCO_3$ export at 100 m this century, with anomalies by 2100 ranging from -74% to $+23\%$ under a high-emission scenario. The greatest export declines are projected by ESMs that consider pelagic $CaCO_3$ production to depend on the local calcite/aragonite saturation state. Despite the potential effects of other processes on alkalinity, there is a robust negative correlation between anomalies in $CaCO_3$ export and salinity-normalized surface alkalinity across the CMIP6 ensemble. Motivated by this relationship and the uncertainty in $CaCO_3$ export projections across ESMs, we perform idealized simulations with an ocean biogeochemical model and confirm a limited impact of carbonate pump anomalies on 21st century ocean carbon uptake and acidification. However, we highlight a potentially abrupt shift, between 2100 and 2300, in the dissolution of $CaCO_3$ from deep to subsurface waters when the global-scale mean calcite saturation state reaches about 1.23 at 500 m (likely when atmospheric CO_2 reaches 900–1100 ppm). During this shift, upper ocean acidification due to anthropogenic carbon uptake induces deep ocean acidification driven by a substantial reduction in $CaCO_3$ deep dissolution following its decreased export at depth. Although the effect of a diminished carbonate pump on global ocean carbon uptake and surface ocean acidification remains limited until 2300, it can have a large impact on regional air–sea carbon fluxes, particularly in the Southern Ocean.

1 Introduction

Plankton are the base of the oceanic food chain, providing both structure and function to marine ecosystems. In addition, by producing organic matter and calcium carbonate – in the case of calcifying plankton – which is exported as particulates to the ocean interior, they act as a biological carbon pump, which is central to understanding the ocean carbon cycle (Hain et al., 2014). Each year, these organisms facilitate the export of about 10 PgC of organic matter and calcium carbonate from the surface ocean to the ocean interior (DeVries

and Weber, 2017; Sulpis et al., 2021), with a range of uncertainty of about 4–16 Pg yr^{-1}. Thus, in the face of increasing atmospheric CO_2 concentration and climate change resulting from human activities, it is crucial to understand the response of these organisms to emerging environmental stressors (e.g. acidification, increased temperature, deoxygenation and reduced nutrient availability) (Kwiatkowski et al., 2020). A particular focus is accorded to the surface ocean where most of the feedback between marine biology and the

global Earth system is expected to occur throughout this century (Canadell et al., 2021).

The soft-tissue and carbonate pumps, which together make up the biological pump, have opposing effects on the surface carbon cycle by modifying dissolved inorganic carbon (DIC) and total alkalinity (Alk) differently (e.g. Zeebe and Wolf-Gladrow, 2001; Sarmiento and Gruber, 2006; Hain et al., 2014). Organic matter production results in CO_2 uptake and a basification of the surface ocean. In contrast, the production of calcium carbonate ($CaCO_3$) causes a release of CO_2 and an acidification of the surface ocean. Hence, the carbonate pump effectively exports carbon from the surface to the ocean interior while promoting a degassing of CO_2 to the atmosphere in what is called the "carbonate counter-pump". While the soft-tissue pump is key in driving the vertical DIC gradient, the carbonate pump, about an order of magnitude smaller in terms of carbon export at 100 m, is important for driving the vertical Alk gradient (Sarmiento and Gruber, 2006; Planchat et al., 2023). One should therefore consider the two pumps separately, particularly with respect to the export of particulate organic carbon (POC) in the case of the soft-tissue pump and of particulate inorganic carbon (PIC) in the case of the carbonate pump. The rain ratio, defined as the ratio between the exports of PIC and POC (e.g. Zeebe and Wolf-Gladrow, 2001), has long been of interest to modellers in their quest for implicit parameterization of the carbonate pump based on the representation of the soft-tissue pump (Planchat et al., 2023). But the rain ratio is also central in assessing the effects of the biological pump on the surface carbon cycle. For instance, relative anomalies of DIC associated with changes in $p\mathrm{CO}_2$ can be quantified using the Revelle factor, which can be expressed as a function of the rain ratio (Zeebe and Wolf-Gladrow, 2001), particularly for making large-scale order-of-magnitude assessments.

In the framework of the Coupled Model Intercomparison Projects (CMIPs), a number of Earth system model (ESM) comparisons have analysed soft-tissue pump projections, typically focusing on net primary production (NPP) and POC export (Bopp et al., 2013; Laufkötter et al., 2015, 2016; Fu et al., 2016; Kwiatkowski et al., 2020; Tagliabue et al., 2021; Henson et al., 2022; Wilson et al., 2022; for CMIP5 and CMIP6). However, no comparison studies exist to date on carbonate pump projections, and especially PIC export. Yet, biological studies carried out on calcifiers raise questions regarding their response to climate change and acidification (Gattuso and Hansson, 2011). Although laboratory and field-data meta-analyses generally support an expected decrease in calcification due to ocean acidification (e.g. Kroeker et al., 2013; Meyer and Riebesell, 2015; Seifert et al., 2020) – especially for planktonic calcifiers, calcifying algae and corals (Leung et al., 2022) – uncertainties are high due to potential decoupling between growth and calcification in response to environmental stressors (e.g. light and nutrient availability, as well as carbonate chemistry; Zondervan et al., 2001; Seifert et al., 2022). In addition, biological studies often focus on

coccolithophores, and in particular *Emiliania huxleyi*, which may not be representative of wider pelagic calcifiers (Ridgwell et al., 2007), which exhibit diverse responses to environmental change (e.g. Kroeker et al., 2013). All these considerations make it difficult to constrain model parameterizations with confidence. Modelling studies carried out to assess the potential feedback of the carbonate pump in response to climate change and acidification have thus shown divergent results essentially depending on the $CaCO_3$ production parameterization. While a climate-driven increase in the future growth rates of certain calcifying species has been projected (Schmittner et al., 2008), a CO_2-driven decrease in calcification in response to ocean acidification has also been projected (Gehlen et al., 2007; Ridgwell et al., 2007; Ilyina et al., 2009; Hofmann and Schellnhuber, 2009; Gangstø et al., 2011; Pinsonneault et al., 2012). The former induces a positive climate feedback as opposed to the latter, emphasizing the potential importance of considering these effects with an explicit representation of calcifiers (Krumhardt et al., 2019). Despite this, all current ESMs implicitly model $CaCO_3$ production based on POC production, and rarely with a saturation-state dependency (Planchat et al., 2023). Models also typically consider calcite and not aragonite production, which may induce delays in the response of the carbonate pump to acidification, as aragonite is less stable than calcite. Similarly, models may underestimate the carbonate pump feedback by not representing benthic calcifiers, such as corals, which are likely to be particularly vulnerable to climate change (Bindoff et al., 2019).

On paleoclimatic timescales, especially for the study of glacial–interglacial transitions, the oceanic $CaCO_3$ cycle is often invoked to explain changes in the global carbon cycle and, in particular, variability in the concentration of atmospheric CO_2 of about 80–100 ppm (Sigman and Boyle, 2000). Changes in the carbonate pump magnitude, in particular through shallow water coral reef surface availability, could partly drive large variations in the concentration of atmospheric CO_2 (e.g. Ridgwell et al., 2003). In addition, in response to a perturbation in carbonate chemistry, the carbonate compensation feedback tends to restore the balance between river input of Alk and $CaCO_3$ burial through fluctuations in the lysocline depth – the upper limit of the transition zone, where sinking and sedimentary $CaCO_3$ starts to substantially dissolve – at a timescale of about 10^4 years (e.g. Broecker and Peng, 1987; Sigman and Boyle, 2000; Sarmiento and Gruber, 2006; Boudreau et al., 2018; Kurahashi-Nakamura et al., 2022). This mechanism alleviates an initial perturbation in atmospheric CO_2 from an external source to the ocean (negative feedback; e.g. for an imbalance in the terrestrial carbon cycle) and amplifies it when resulting from an internal ocean process (positive feedback; e.g. for a change in the organic matter or $CaCO_3$ production; Sarmiento and Gruber, 2006).

In this study, we are interested in how the future carbonate pump, as simulated in ESMs, responds to the anthropogenic

perturbation of the carbon cycle, the speed and amplitude of which are greater than those of glacial–interglacial transitions. We also explore the feedback associated with this modification to the oceanic carbon cycle on multi-centennial timescales. To do so, we compare PIC export projections under high 21st century anthropogenic emissions in the CMIP6 model ensemble. Finally, to gain insight into the potential influence of PIC export biases and trends on projections of future ocean carbon uptake and acidification, we perform sensitivity simulations using the NEMO-PISCES marine biogeochemical model.

2 Methodology

2.1 CMIP6 ESMs and outputs

We assess 15 ESMs from 12 different climate modelling centres (CCCma, CMCC, CNRM-CERFACS, CSIRO, IPSL, MIROC, MOHC, MPI-M, MRI, NCAR, NCC and NOAA-GFDL), which took part in the sixth phase of the Climate Model Intercomparison Project (CMIP6; Eyring et al., 2016). All ESMs considered in this study represent the carbonate pump with the production of pelagic $CaCO_3$, its export in the form of PIC, as well as its dissolution and potential burial at depth. While we analysed only one ensemble member per ESM, we assessed two distinct ESMs for MPI-M since two different resolutions were available, as well as for CCCma and NOAA–GFDL for which two distinct marine biogeochemical models were available (see Table A1). For each of the ESMs, we considered the pre-industrial control simulation (piControl), the historical scenario (hereafter referred to as "Historical", covering the recent past from 1850 to 2014) and the two extreme CMIP6 Shared Socioeconomic Pathways (SSPs), i.e. SSP1-2.6 and SSP5-8.5. While our focus is on the SSP5-8.5 scenario, we use the SSP1-2.6 scenario, not available for MRI-ESM2-0 and GFDL-CM4, as a point of comparison. Each ESM is weighted in the calculation of CMIP6 statistical values (mean, standard deviation, quartiles and linear regressions) such that each modelling group has the same total contribution.

The following variables were processed when available: (i) two-dimensional (2D) variables, i.e. sinking fluxes at 100 m of organic matter, calcite and aragonite (respectively, "epc100", "epcal100" and "eparag100") and the CO_2 gas exchange between the ocean and the atmosphere ("fgCO$_2$"); and (ii) three-dimensional (3D) variables, i.e. total alkalinity ("talk"), dissolved inorganic carbon ("dissic"), phosphate and silicate concentrations ("po4" and "si"), salinity ("so") and potential temperature ("thetao"). In order to facilitate the ESM intercomparison, we used the distance-weighted average remapping "remapdis" and linear level interpolation with extrapolation "intlevelx" of the Climate Data Operator (CDO) tool to regrid the data on a regular $1° \times 1°$ grid with 33 depth levels from 5 to 5500 m. The ocean carbonate system was computed with mocsy 2.0 (Orr and Epitalon, 2015)

over the simulation period using annual (i) Alk, DIC, salinity and temperature from ESM outputs, (ii) phosphate and silicate from ESMs or from the gridded observational-based product of the Global Ocean Data Analysis Project (GLO-DAPv2.2020, Olsen et al., 2020) if at least one of the two was not simulated and (iii) the seawater equilibrium constants recommended for best practices (Dickson et al., 2007; Orr and Epitalon, 2015). Quality control of ESM outputs led us to (i) exclude grid cells with a salinity lower than $25\,\mathrm{g\,kg^{-1}}$ in the analysis of processes including salinity data due to salinity normalization issues, and (ii) restrict the CNRM-ESM2-1 domain to exclude grid cells in the Japan Sea that exhibit highly anomalous PIC export.

2.2 NEMO-PISCES ocean biogeochemical model and sensitivity simulations

We used the marine biogeochemical model NEMO-PISCES to evaluate how a steady-state bias, or a change in the carbonate pump magnitude, can impact the ocean carbon cycle in the Anthropocene, suggested to start at the time of the Industrial Revolution (Crutzen and Stoermer, 2000). Although this model is globally similar to the PISCES version described in Aumont et al. (2015), and used in IPSL-CM6A-LR, we made two changes: (i) the N-fixation parameterization was modified following Bopp et al. (2022) and (ii) the burial fraction of PIC was adjusted so that the global Alk inventory was conserved without the need of an Alk restoring scheme (see Appendix A2). In NEMO-PISCES, PIC production does not depend on the local saturation state; however, PIC dissolution linearly depends on the saturation state, whether in the water column or at the ocean floor (Planchat et al., 2023).

We performed offline simulations on a tripolar ORCA grid with a nominal resolution of $2°$ and 30 vertical levels. While keeping pre-industrial ocean physics from an ESM used in CMIP5 by IPSL (IPSL-CM5A-LR; Dufresne et al., 2013), we completed 500-year runs (from 1800 to 2299) with the atmospheric CO_2 concentration following that of the Historical and then the Representative Concentration Pathway (RCP) 8.5 scenario. Although slightly less extreme than the SSP5-8.5 scenario, reaching 936 ppm in 2100 as opposed to 1135 ppm for the latter (see Appendix A3), this approach suited this analysis by validating orders of magnitude while using relatively coarse resolution simulations with low computational cost, as the CMIP6 scenarios were only available at higher resolution for the IPSL ESM. Two configurations with varying carbonate pump magnitudes were brought to steady state with a 2500-year spin-up, during which the burial fraction of PIC is free to evolve, prior to being fixed at the end of the spin-up (see Table A2).

We performed two sensitivity simulations in parallel. First, we extended the two simulations brought to equilibrium according to the Historical and RCP8.5 scenario (referred to as "standard" and "carb_low" herein) to assess the consequences of an equilibrium bias in the amplitude of the car-

bonate pump. Second, we performed two simulations for which we imposed a decrease or an increase (respectively referred to as "carb–" and "carb+" herein) of the carbonate pump as a function of the atmospheric CO_2 concentration in order to estimate the impact of a variation in the carbonate pump magnitude on the carbon cycle. In both simulations, the PIC production in the model was multiplied by $(1-\alpha_{carb})$ for carb– and $(1+\alpha_{carb})$ for carb+ with

$$\alpha_{carb} = \frac{1}{3} \cdot \frac{CO_2{}^{atm} - 285}{936 - 285}, \tag{1}$$

where 285 ppm is the atmospheric CO_2 concentration in 1850 and 936 ppm is the concentration in 2100 under RCP8.5. A dependency on the atmospheric CO_2 concentration was preferred to a saturation state dependency to avoid any feedback from PIC production on the saturation state, which in turn influences PIC production itself. This also permitted control of the PIC production values reached in the sensitivity experiments so that they could be directly compared with one another and with the CMIP6 ensemble. Additional sensitivity simulations of the standard configuration were performed in support of the main analysis, taking into account only climate-driven effects (referred to as "standard_dyn") or both climate-driven and CO_2-driven effects (referred to as "standard_dyn+atm"; see Table A2).

2.3 Technical processing

We used the normalization approach of dividing surface Alk and DIC values by the coincident salinity and multiplying this by a reference salinity value of $35 \, \text{g kg}^{-1}$ (e.g. Sarmiento and Gruber, 2006; Fry et al., 2015) to remove the impact of freshwater fluxes (e.g. precipitation, evaporation, sea ice formation/melting and river discharge; Friis et al., 2003). Hereafter, salinity-normalized Alk and DIC are referred to as "sAlk" and "sDIC", respectively. A sAlk drift threshold of $2 \, \text{mmol m}^{-3}$ per century was used to exclude models when reporting ESM values that may be affected by such a drift. This criterion thus excludes CMCC-ESM2 and CNRM-ESM2-1, due to a salinity drift for the former and an Alk drift for the latter (see Appendix A5).

In the following, we refer to $CaCO_3$ without distinguishing between calcite and aragonite, unless explicit. This distinction is only relevant for GFDL-ESM4, which is the only ESM to represent both calcite and aragonite in CMIP6. In contrast, most groups simulate only calcite, whereas ACCESS-ESM1-5 simulates a generic $CaCO_3$. Moreover, as calcite is the calcium carbonate mineral most commonly considered in ESMs, we use the calcite saturation state as a proxy for ocean acidification. We also define the rain ratio at 100 m as the ratio of the spatially integrated PIC and POC exports at 100 m.

Furthermore, we did not de-bias the simulated carbonate chemistry of both ESM and NEMO-PISCES runs in order to maintain consistency in the physicochemistry experienced by marine biogeochemical processes within each model. We applied 11-year rolling means to the time series, and when considering absolute values or anomalies, we averaged over 20-year periods to limit the influence of interannual variability which can be considerable for PIC export.

3 Results and discussion

3.1 Divergent PIC export projections in CMIP6 ESMs

The 21st century projections of PIC export are highly divergent (from -74% to $+23\%$ for 2081–2100 for SSP5-8.5; Fig. 1a) in CMIP6 ESMs, while projections of POC export are more consistent (-21% to $+3\%$; see Fig. B3b). The divergent trend in the rain ratio (from -69% to $+30\%$; Fig. 1b) is therefore predominantly controlled by changes in PIC export. Nonetheless, the maximum end-of-the-century projected changes in PIC export ($-0.40 \, \text{PgC yr}^{-1}$) and the rain ratio ($-0.053$) under SSP5-8.5 are smaller than the inter-model ranges of pre-industrial PIC export and rain ratios across the CMIP6 ensemble (respectively from 0.40 to $1.18 \, \text{PgC yr}^{-1}$, and from 0.040 to 0.132).

The divergent PIC export projections are essentially explained by UKESM1-0-LL, GFDL-CM4 and GFDL-ESM4 (Fig. 1a). These are the only ESMs that include a linear dependency of PIC production on the local saturation state (see the description of their biogeochemical models, MEDUSA-2.1, BLINGv2 and COBALTv2, in Planchat et al., 2023). Through the absorption of anthropogenic carbon, the upper ocean acidifies, the saturation state decreases and calcification therefore declines in these ESMs over SSP5-8.5 (respectively by -71.4%, -73.5% and -73.1% for 2081–2100; Fig. 1a). Interestingly, for the only ESM in CMIP6 that represents both implicit calcite and aragonite production, GFDL-ESM4, the decline in aragonite export (-80.3%) is only slightly higher than that of calcite export (-71.6%), despite the higher solubility of aragonite.

For the other ESMs, PIC export trends are less divergent, but even the sign of change is unclear, with ESMs projecting increases of up to $+22.8\%$ and decreases of up to -17.4% for 2081–2100. For these ESMs, there is a positive correlation between changes in PIC and POC export anomalies ($R^2 = 0.65$, $p < 0.01$; Fig. 3a). This is unsurprising given that PIC production is typically parameterized using a production ratio based on POC production (Planchat et al., 2023). As a result, the spatial patterns of PIC and POC export changes are also highly positively correlated for 2081–2100, with general declines at low latitudes partially offset by increases at high latitudes (see Figs. B2b–d and B3c–e).

Historical and SSP5-8.5 scenarios relative to pre-industrial control
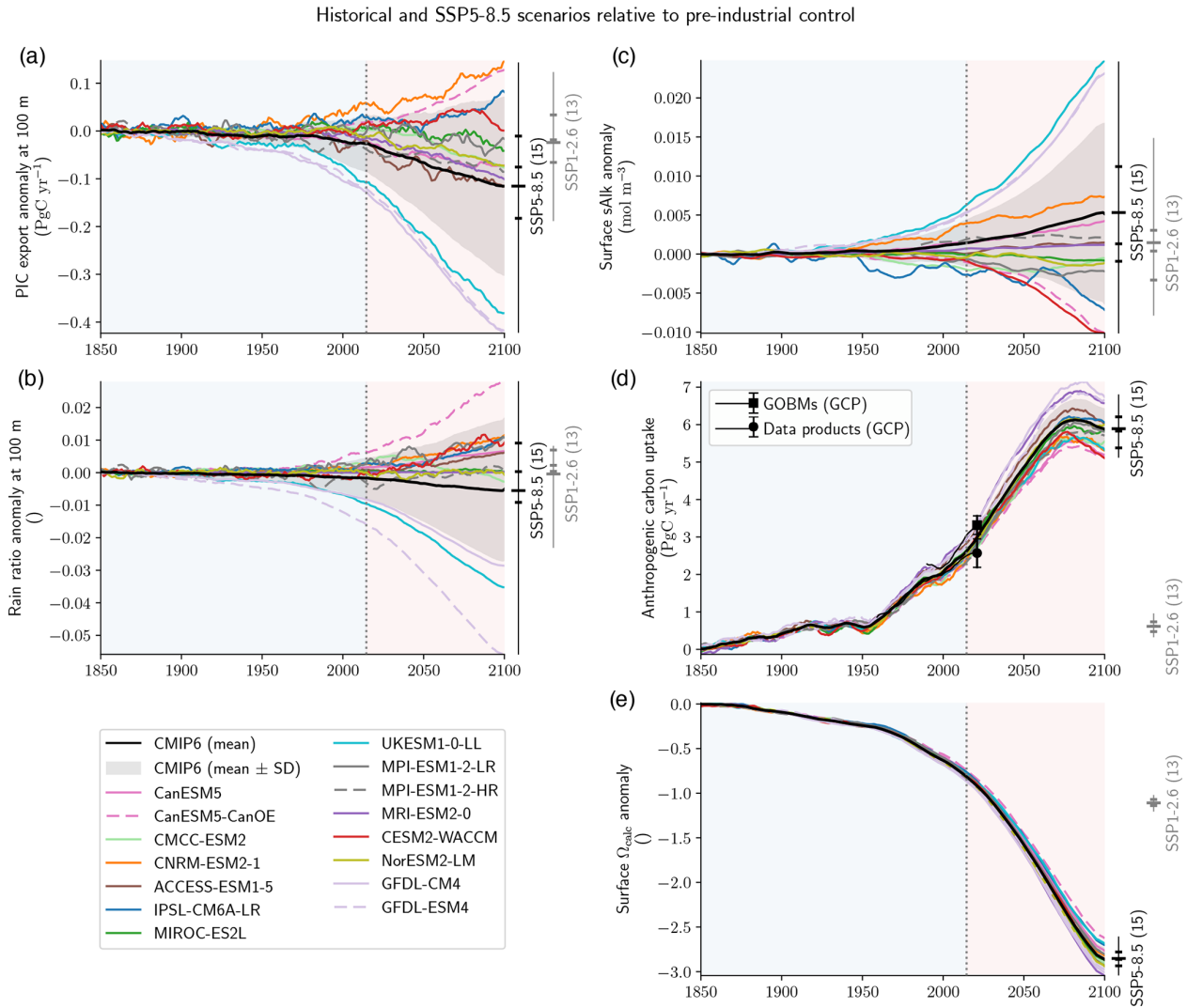
Figure 1. ESM projections of PIC export, ocean carbonate chemistry and anthropogenic carbon uptake. ESM projected anomalies relative to the pre-industrial control simulation in **(a)** PIC export at 100 m, **(b)** the rain ratio at 100 m, **(c)** surface sAlk, **(d)** anthropogenic carbon uptake and **(e)** surface calcite saturation state in the Historical and SSP5-8.5 simulations. For each panel, the data are smoothed with 11-year rolling means, and the number of ESMs available, means, quartiles and extreme values for 2100, for both SSP5-8.5 and SSP1-2.6, are provided. Assessments of the 2021 anthropogenic ocean carbon uptake are based on data products and global ocean biogeochemical models (GOBMs), with their associated standard deviation provided (Global Carbon Project, GCP; Friedlingstein et al., 2022).

3.2 Limited 21st century impact of PIC export on ocean carbon uptake and acidification

3.2.1 Insights from NEMO-PISCES sensitivity simulations

The NEMO-PISCES simulations were designed to assess the potential impact of CMIP6 carbonate pump biases and projection uncertainties (see Table A2). The simulated PIC export is $1.16\,\mathrm{Pg\,C\,yr^{-1}}$ in the standard simulation and $0.81\,\mathrm{Pg\,C\,yr^{-1}}$ in the carb_low simulation under pre-industrial conditions, in both cases remaining almost unchanged under increasing atmospheric CO_2 concentration from 1850 to 2100. In contrast, and as expected from the

simulation set-up (see "Methodology" above), PIC export declines in carb– from 1.16 to $0.87\,\mathrm{Pg\,C\,yr^{-1}}$ for 2081–2100 ($-25\,\%$), while in carb+ it increases to $1.50\,\mathrm{Pg\,C\,yr^{-1}}$ ($+29\,\%$). The difference between the standard and carb_low PIC export values encompasses CMIP6 biases in steady-state PIC export values, while the PIC export anomalies simulated in carb– and carb+ encompass CMIP6 anomalies under SSP5-8.5 (Fig. 2a). In all NEMO-PISCES simulations, the POC export is identical and near constant over the period 1850–2100 ($8.50\,\mathrm{Pg\,C\,yr^{-1}}$).

By maintaining pre-industrial ocean temperature and circulation throughout the NEMO-PISCES simulations, surface sAlk responds directly to the changes in PIC ex-
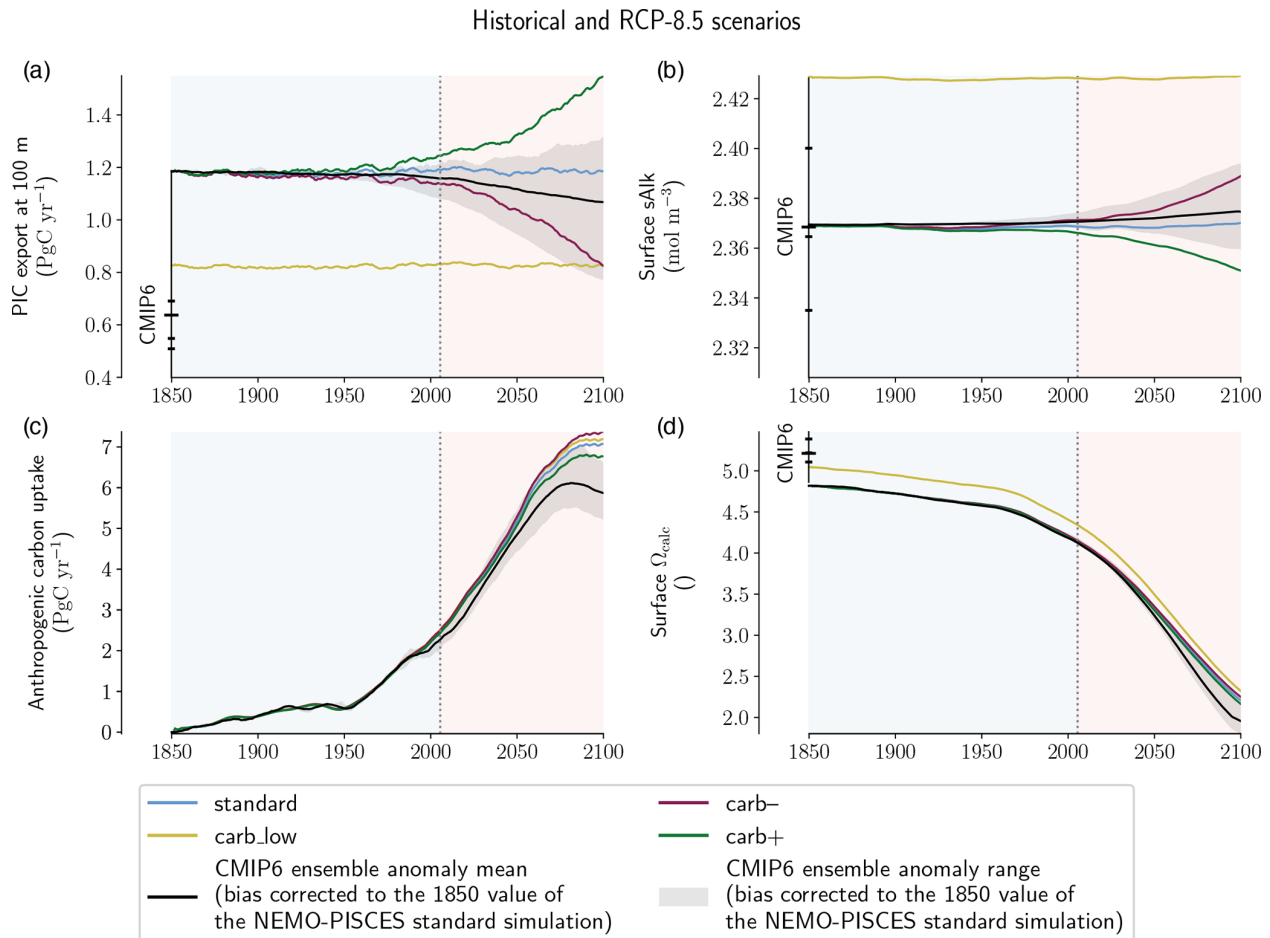
Figure 2. NEMO-PISCES sensitivity simulations. Absolute values of **(a)** PIC export at 100 m, **(b)** surface sAlk, **(c)** anthropogenic carbon uptake and **(d)** surface calcite saturation state. For each panel, the data are smoothed with 11-year rolling means and CMIP6 ensemble statistical elements (mean, quartiles and extreme values) are provided for early Historical experiment values for 1850. The CMIP6 ensemble anomaly mean (black line) and range (grey shading) are shown bias corrected to the 1850 value of the NEMO-PISCES standard simulation.

port and not to other processes (Fig. 3b). Due to the effect of calcification on Alk, sAlk increases when PIC export declines, and vice versa. Thus, using carb− and carb+, a characteristic global relationship can be inferred between PIC export and surface sAlk anomalies (slope: -5.12×10^{-2} mol m^{-3} (Pg C yr^{-1})$^{-1}$; $p < 0.01$; Fig. 3b).

The relative effect of changes in PIC export on 2081–2100 projections of anthropogenic ocean carbon uptake is small ($+0.25$ Pg C yr^{-1} for carb− and -0.26 Pg C yr^{-1} for carb+; $+4.0\%$ and -4.1%, respectively) and near negligible with regard to surface Ω_{calc} ($+0.039$ for carb− and -0.039 for carb+ ; $+1.6\%$ and -1.6%, respectively; Fig. 3c and d). Yet, by constraining the PIC export change in response to rising atmospheric CO_2 concentration in carb− and carb+, a high-end assessment of the carbonate pump impact is obtained. Indeed, a decrease in PIC production would lead to a relative basification of the surface ocean, and thus to a dampening of the acidification related to the increase in atmospheric CO_2 concentration, i.e. a negative feedback. However, it should be

noted that the relative change in anthropogenic carbon uptake is of the same order of magnitude as the absolute change in PIC export (e.g. 0.25 versus 0.29 Pg C yr^{-1} for carb−), illustrating a simple quantitative relationship between PIC export changes and carbon uptake.

The impact of a negative bias in the mean-state PIC export (carb_low compared with standard) is limited for anthropogenic ocean carbon uptake ($+0.13$ Pg C yr^{-1}; $+2.0\%$) and relatively small with respect to surface acidification (-0.125 for Ω_{calc}; -5.2%; Fig. 3c and d). Indeed, at global scale, for the same atmospheric CO_2 concentration increase, the associated rise in DIC is more important for carb_low than the standard simulation. This is essentially driven by a greater ratio between surface DIC and the Revelle factor (Revelle and Suess, 1957) – directly connecting an absolute change in surface DIC to a relative change in atmospheric CO_2 – for carb_low compared with the standard simulation. As surface sAlk remains stable for these two simulations, this leads to higher carbon uptake and greater associated acidifi-
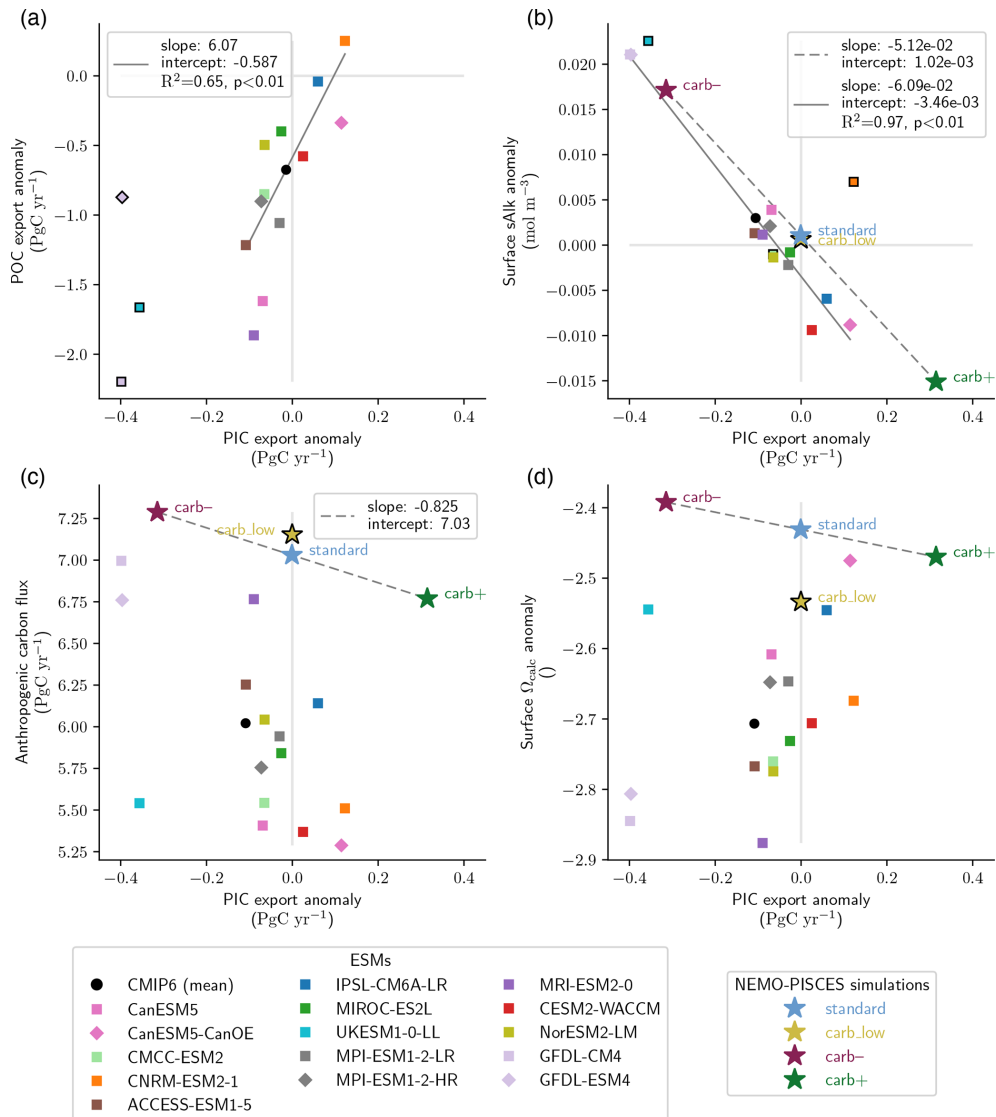
Figure 3. Relationships between PIC export and POC export, ocean carbon uptake, surface alkalinity and acidification. Simulated PIC export anomalies at 100 m and the corresponding **(a)** POC export anomalies at 100 m, **(b)** surface sAlk anomalies, **(c)** ocean anthropogenic carbon flux and **(d)** surface calcite saturation state. Anomalies are calculated for 2081–2100 relative to the piControl experiments. Linear regressions of NEMO-PISCES simulations (dashed grey lines) are calculated using the standard, carb– and carb+ simulations. The carb_low simulation is excluded (indicated with black-bordered symbols) as its initial state differs from that of the other simulations. CMIP6 ensemble linear regressions (solid grey lines) are calculated excluding the ESMs shown with a black-bordered symbol. In **(a)**, UKESM1-0-LL, GFDL-CM4 and GFDL-ESM4 are excluded as they consider a saturation state dependency for PIC production, leading to substantial differences in PIC export anomalies compared with the other ESMs. In **(b)**, CMCC-ESM2 and CNRM-ESM2-1 are excluded due to their surface sAlk drift (see Sect. 2.3) and UKESM1-0-LL is excluded because it omits the influence of the soft-tissue pump on sAlk (see Appendix B1).

cation over the period compared with the standard simulation (Fig. 3b).

The climate change feedback on ocean carbon uptake and surface acidification far outweighs the acidification-driven change in the carbonate pump (see Fig. B4e and f). When including all climate change effects, and in particular changes in ocean temperature and circulation (standard_dyn+atm simulation), the anthropogenic carbon uptake decreases by

$1.38\,\mathrm{PgC\,yr^{-1}}$ and Ω_{calc} increases by 0.363 for 2081–2100 relative to the standard simulation (respectively $-19.6\,\%$ and $+15.2\,\%$). This response has been extensively studied using a variety of ocean-only models and ESMs for more than two decades (Sarmiento et al., 1998; Schwinger et al., 2014; Arora et al., 2020; Canadell et al., 2021). These effects result from a combination of climate-change impacts on anthropogenic carbon uptake through changes in the physical (main

driver) and biological pumps with decreased solubility, increased stratification and decreased ventilation (e.g. Canadell et al., 2021).

Building on the NEMO-PISCES sensitivity simulations, we can assess the potential extent to which PIC export anomalies may influence surface sAlk, anthropogenic carbon uptake and surface acidification in CMIP6 ESM projections, and over which timescales.

3.2.2 Minimal influence in CMIP6 ESM projections

The analysis of the CMIP6 ensemble confirms the robust negative relationship between the PIC export and surface sAlk anomalies by the end of the century (Fig. 3b). As with projections of PIC export, UKESM1-0-LL, GFDL-CM4 and GFDL-ESM4 stand out with significant increases in surface sAlk (respectively +0.022, +0.021 and +0.021 $mol\,m^{-3}$) for 2081–2100 under SSP5-8.5 (Fig. 1c). For the other ESMs, the sign of the anomaly remains uncertain, showing either an increase (up to +0.007 $mol\,m^{-3}$) or a decrease (up to $-0.009\,mol\,m^{-3}$). At the end of the century, a variation in the amplitude of the PIC export is matched by a proportional variation in surface sAlk (slope: $-6.09 \times 10^{-2}\,mol\,m^{-3}\,(Pg\,C\,yr^{-1})^{-1}$; $R^2 = 0.97$, $p < 0.01$), similar to the relationship identified across the NEMO-PISCES simulations (Fig. 3b). Even when excluding ESMs with a large decrease in PIC export, we still find a significant correlation between PIC export changes and surface sAlk changes ($R^2 = 0.80$, $p < 0.01$). Thus, the divergent PIC export projections drive contrasting trends in surface sAlk across the CMIP6 ensemble, with ESMs that project a large decrease in PIC export consistently projecting increases in surface sAlk. PIC export, in addition to being the main driver of the quasi-steady-state vertical sAlk gradient (Planchat et al., 2023), therefore drives surface sAlk anomaly projections this century. As a result, there is some confidence in using observations of salinity-normalized surface Alk to identify trends in PIC export at 100 m, and thus of the carbonate pump until at least 2100 (Ilyina et al., 2009).

Interestingly, this relationship is robust despite the effect of POC export and circulation changes on Alk (see Appendix B1). Although the POC export anomaly in ESMs is, in absolute terms, 0.7–35 times larger than the PIC export anomaly (see Fig. B3b compared with Fig. 1a), changes in PIC export still drive surface sAlk anomalies. As a global decrease in POC export is projected in the CMIP6 ensemble, the effect of this change in the soft-tissue pump on surface sAlk could explain the negative intercept of the relationship obtained for the ESMs, since a negative POC export anomaly would drive a negative surface Alk anomaly (see Appendix B1). In addition, the positive relationship between PIC and POC exports (Fig. 3a) would tend to slightly increase the negative slope of the sAlk–PIC export relationship, as a decline in POC export would act to enhance declines in PIC export resulting in a greater decrease in sur-

face sAlk (see Appendix B1b). Thus, the representation of the soft-tissue pump, from organic matter production to remineralization, has limited effects on the relationship between PIC export and surface sAlk anomalies.

ESMs also show differences in carbon uptake and surface ocean acidification from 1850 to 2100 (Fig. 1d and e). The trend shown is consistent for the CMIP6 ensemble, although a dispersion of the ESMs persists and increases over the century under SSP5-8.5, especially for the anthropogenic carbon flux. The values for the anthropogenic carbon uptake for 2081–2100 under SSP5-8.5 range from 5.29 to 6.99 $Pg\,C\,yr^{-1}$, and for Ω_{calc} they range from -2.87 to -2.46. These ranges are larger than those obtained for our idealized sensitivity simulations, ranging from 6.77 to 7.29 $Pg\,C\,yr^{-1}$ for the anthropogenic carbon uptake and from 2.35 to 2.43 for Ω_{calc}. While these signals are mostly driven by the ability of the surface ocean to respond to the increase in atmospheric CO_2, there is no inter-ESM correlation between PIC export anomalies and either ocean carbon uptake or surface ocean acidification. Thus, only a limited fraction of the differences in anthropogenic carbon uptake and surface ocean acidification in the CMIP6 ensemble can be explained by changes in the carbonate pump.

3.3 Enhanced post-2100 impact of PIC export anomalies on the ocean carbon cycle

The relationship between PIC export and surface sAlk anomalies in the extended NEMO-PISCES simulations substantially changes post-2100 (Fig. 4a). While PIC export declines have a slightly greater impact on changes in sAlk (slope: $-6.84 \times 10^{-2}\,mol\,m^{-3}\,(Pg\,C\,yr^{-1})^{-1}$ for 2270–2299 compared with $-5.12 \times 10^{-2}\,mol\,m^{-3}\,(Pg\,C\,yr^{-1})^{-1}$ for 2081–2100), what is the most striking is a general increase in surface sAlk. This increase in sAlk even occurs for the standard and carb_low simulations that exhibited near-stable surface sAlk until 2100 (+0.056 $mol\,m^{-3}$ for standard and +0.038 $mol\,m^{-3}$ for carb_low from 2100 to 2300; +2.4 % and +1.6 %). As a result, the intercept of the regression between PIC export and surface sAlk anomalies is shifted towards higher values by 2300 (from $1.02 \times 10^{-3}\,mol\,m^{-3}$ for 2081–2100 to $5.27 \times 10^{-2}\,mol\,m^{-3}$ for 2270–2299).

This general increase in surface sAlk responds to an abrupt shift in the vertical $CaCO_3$ dissolution pattern following the shoaling of the saturation horizon in response to long-term ocean acidification (Fig. 4b and c). While dissolution is mainly confined to deep waters (> 1500 m) and essentially the sediment interface prior to 2100, by around 2150 it almost entirely occurs in the subsurface (< 1500 m) under high emissions. This dissolution predominantly occurs in the water column and no longer at the seafloor. The dependence of dissolution on the saturation state in NEMO-PISCES (Aumont et al., 2015) – utilized in about half of the CMIP6 ESMs (Planchat et al., 2023) – therefore drives a sudden shift in PIC dissolution depth, impacting surface sAlk. Indeed, the
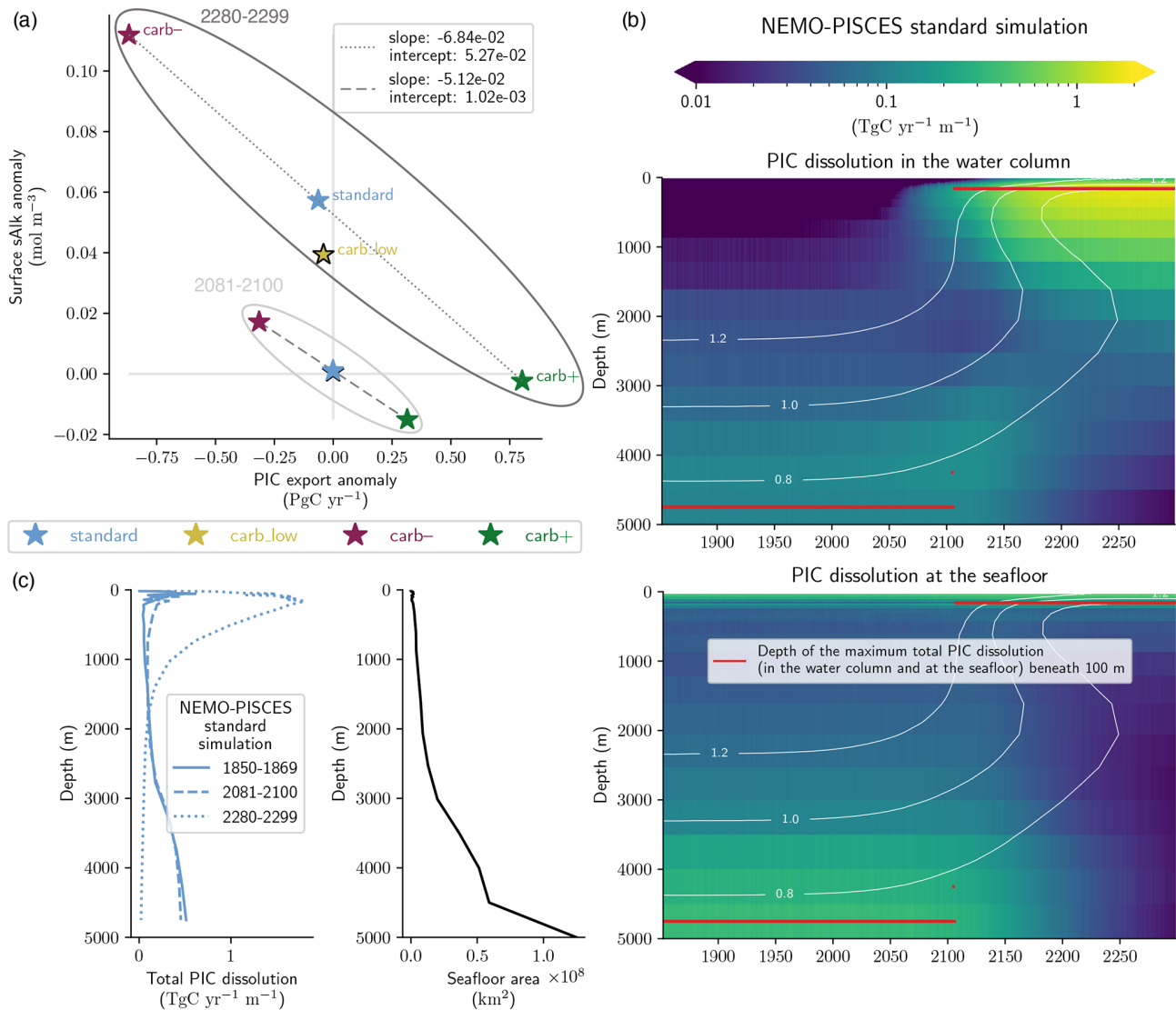
Figure 4. Multi-centennial effects of acidification on the global carbonate pump under high emissions for the NEMO-PISCES sensitivity simulations. Panel **(a)** shows the relationship between PIC export anomalies at 100 m and surface sAlk anomalies for 2280–2299 and 2081–2100 (as in Fig. 3b). Linear regressions (dashed and dotted grey lines) are calculated using the standard, carb– and carb+ simulations (excluding carb_low, indicated with a black-bordered star). Panel **(b)** shows global PIC dissolution with depth both within the water column (top) and at the seafloor (bottom) for the NEMO-PISCES standard simulation. Calcite saturation state contours are displayed at 0.8, 1.0 and 1.2. The depth of maximum total PIC dissolution (i.e. the sum of water column and benthic dissolution) below 100 m – as a high quantity of PIC is produced and dissolved in shallow waters in NEMO-PISCES – is shown in red. Panel **(c)** shows the evolution of the total PIC dissolution profile in a high-emission scenario with a mirrored bathymetric profile to highlight the extent of the seafloor according to depth.

shift is the consequence of the strong anthropogenic ocean acidification signal that slowly propagates towards the bottom from the surface. The subsurface ocean thus tends to be undersaturated before part of the ocean interior. A general increase in surface Alk has previously been reported in other model simulations, but it was attributed to increased seafloor dissolution due to ocean acidification (Ilyina et al., 2009) rather than a shift from seafloor to water column dissolution. Furthermore, this shift could be even more abrupt, and CaCO$_3$ dissolution further confined to surface waters if

the parameterized saturation state dependency of CaCO$_3$ dissolution were non-linear, as suggested by laboratory studies, which indicate an exponent >1 for PIC dissolution in the water column (e.g. Subhas et al., 2015).

This abrupt shift in the vertical CaCO$_3$ dissolution pattern occurs regardless of the PIC export magnitude at quasi-steady state and its projected anomaly. Indeed, for all the NEMO-PISCES sensitivity simulations, it occurs at the beginning of the 21st century, when global mean Ω_{calc} at 500 m reaches 1.23 ± 0.01. It is reached between 2100 (carb_low)

and 2109 (carb−), corresponding to an atmospheric CO_2 concentration of 936 and 1021 ppm, respectively. A drastic reduction in PIC production only minimally increases the concentration of atmospheric CO_2 coincident with this Ω_{calc} threshold (1021 ppm for carb− versus 1002 ppm for standard), while a weaker steady-state carbonate pump lowers the coincident atmospheric CO_2 concentration (936 ppm for carb_low). This calcite saturation state threshold is consistent in a high-emission scenario, irrespective of ocean circulation. When also considering the effects of climate change on ocean circulation (standard_dyn+atm simulation), the threshold is reached a decade later, due to dampened ocean acidification (see Fig. B4f), occurring at an atmospheric CO_2 concentration of 1088 ppm. As such, the simulated shift in the dissolution pattern is robust and dependent on a specific calcite saturation state threshold. However, the atmospheric CO_2 concentration at which this threshold is crossed depends on the strength and anomaly of the carbonate pump as well as ocean circulation. This shift in the vertical distribution of PIC dissolution is likely reversible if subsurface Ω_{calc} returns to values higher than the threshold (Chen et al., 2021).

The reduction in deep ocean $CaCO_3$ dissolution results in deep ocean acidification, which could regionally occur prior to the penetration of substantial anthropogenic carbon into the ocean interior (Fig. 4b). Indeed, in addition to surface acidification (−2.43 for 2081–2100 and −3.60 for 2280–2299 for Ω_{calc}), deep ocean acidification occurs post-2100 (−0.04 for 2081–2100 and −0.29 for 2280–2299 for Ω_{calc} at 4750 m). In contrast to the direct acidification associated with ocean carbon uptake, this indirect acidification rises from the deep ocean towards the surface (Fig. 4b). It could therefore cause, earlier than expected, deep ocean acidification in regions such as the North Pacific, where the transport of anthropogenic carbon into the deep takes hundreds to thousands of years (e.g. Levin and Le Bris, 2015).

Between 2100 and 2300, the simulated $CaCO_3$ cycle exerts a weak negative feedback on the surface ocean, slightly dampening acidification and increasing carbon uptake, but a positive feedback in the deep ocean, where it enhances acidification. However, it could also trigger a compensatory effect at the seafloor by deepening the lysocline, and inducing a dissolution of sedimentary $CaCO_3$ (not currently represented in NEMO-PISCES), dampening the acidification signal in the deep ocean. Moreover, the shoaling of $CaCO_3$ dissolution raises questions about the impact that this would have if there were a protective and/or ballast effect of $CaCO_3$ on organic matter (e.g. Klaas and Archer, 2002; Passow and De La Rocha, 2006; De La Rocha and Passow, 2007; Lee et al., 2009; Engel et al., 2009; Moriceau et al., 2009). If such an effect is confirmed, enhanced subsurface PIC dissolution would increase the remineralization of subsurface POC, leading to subsurface ocean acidification, which would counteract the associated effect of reduced CO_2 uptake.

Post-2100 changes in the carbonate pump are heightened and regional variability in the air–sea carbon flux is enhanced

(Fig. 5). Although the sAlk and Ω_{calc} anomalies associated with changes in PIC export at 100 m are quite homogeneous, with enhanced anomalies at low to mid latitudes, the air–sea carbon flux response is local and strongly connected to PIC export anomalies. For 2081–2100, in a region where PIC production and thus PIC export decline, there is enhanced ocean carbon uptake. However, for 2280–2299, alongside the increase in ocean carbon uptake due to a more pronounced decline in PIC export, there are also regions of reduced ocean carbon uptake, notably in the Southern Ocean. Up to 2100, changes in the surface carbonate pump are the dominant driver of changes in ocean carbon uptake, acidification and sAlk (Fig. 5a–d). However, by 2300, the impact of upwelled deep waters that have experienced less PIC dissolution is also evident at high latitudes (Fig. 5e–h). This results in high latitude declines in ocean carbon uptake which explains why, beyond 2150, the anthropogenic carbon uptake difference between carb− and carb+ is reduced (see Fig. B4e).

4   Conclusion and perspectives

The projected 21st century response of $CaCO_3$ export in the CMIP6 ensemble is highly divergent under high emissions (ranging from −74 % to +23 %). The ESMs with the largest export declines (< -70 %) all parameterize pelagic $CaCO_3$ production as a function of saturation state, highlighting the need for parameterization consensus to constrain PIC export projections. $CaCO_3$ export also drives divergent projections of the rain ratio and salinity-normalized surface alkalinity across the CMIP6 ensemble. As a robust negative correlation exists between projected anomalies of $CaCO_3$ export and salinity-normalized surface alkalinity in the CMIP6 ensemble, salinity-normalized surface alkalinity observations could be used to identify trends in PIC export, with signals expected to emerge from time series data in the coming decade or so (Carter et al., 2016).

Sensitivity simulations performed with the marine biogeochemical model NEMO-PISCES confirm the limited impact of the carbonate pump on anthropogenic carbon uptake and ocean acidification in the 21st century. Improving the realism of the representation of this carbon pump therefore does not appear to be a priority for constraining uncertainties in anthropogenic carbon uptake and ocean acidification. Nevertheless, on multi-centennial timescales, the effects of a perturbation in the carbonate pump on the carbon cycle are heightened. In particular, a global-scale threshold for the oceanic $CaCO_3$ cycle is highlighted with an abrupt change in the vertical pattern of $CaCO_3$ dissolution from the deep ocean to the subsurface when the global-scale mean calcite saturation state reaches about 1.23 at 500 m (likely when atmospheric CO_2 reaches 900–1100 ppm). The subsurface acidification signal can lead to a deep ocean $CaCO_3$-induced acidification signal post-2100 due to the collapse of $CaCO_3$ dissolution at depth. The effects of these changes on carbon
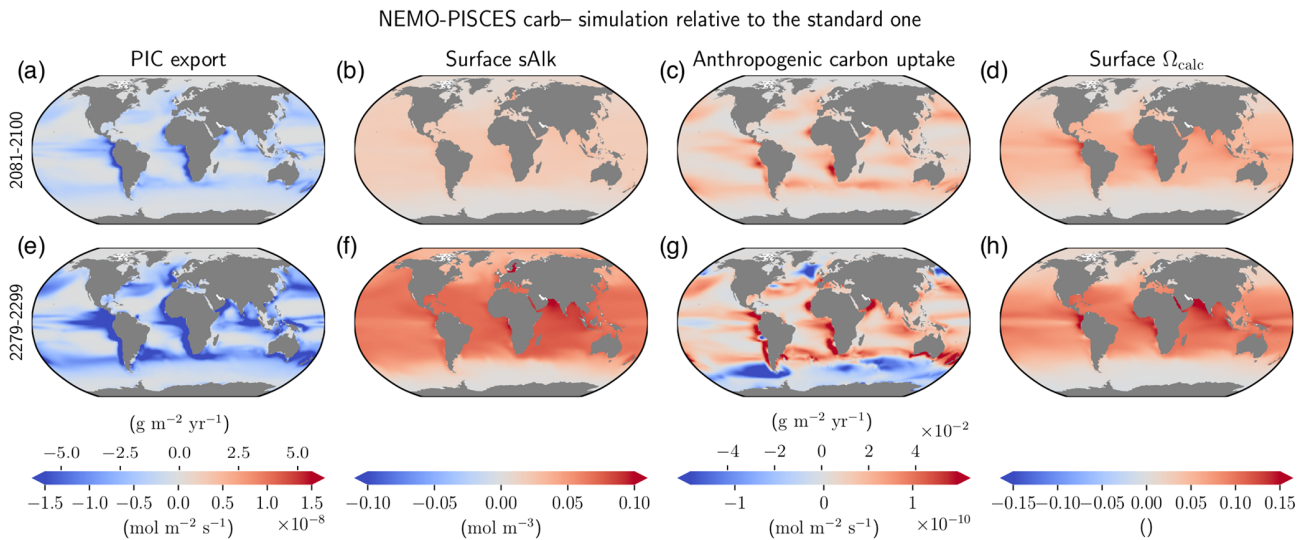
Figure 5. Regional differences in the multi-centennial impact of a declining carbonate pump on ocean carbon uptake and acidification. carb– anomalies of **(a, e)** PIC export at 100 m, **(b, f)** surface sAlk, **(c, g)** anthropogenic carbon uptake and **(d, h)** surface Ω_{calc} relative to the standard simulation, for 2081–2100 **(a–d)** and 2280–2299 **(e–h)**.

uptake and surface ocean acidification remain limited, despite the appearance of regional variability in air–sea carbon fluxes, with upwelled deep waters oppositely impacted by a change in PIC export relative to surface waters.

At present, the physical carbon pump plays the main role in anthropogenic ocean carbon uptake and acidification (Canadell et al., 2021). However, under high emissions the physical carbon pump is likely to saturate before the end of the century due to declining ocean buffer capacity and reduced ocean ventilation (Canadell et al., 2021; Chikamoto et al., 2023). Changes in the biological carbon pump, including the carbonate pump, post-2100 are therefore likely to have a more important feedback on anthropogenic carbon uptake and acidification. Although projected declines in the carbonate pump have limited impact on global climate and ocean acidification this century, such declines may still have important local ecosystem impacts.

Appendix A: Methodology

A1   CMIP6 ESMs

Details regarding the ESMs considered in this analysis are given in Table A1.

A2   Conservation of the global Alk inventory

Historically, NEMO-PISCES was configured with annual Alk restoration to keep its global inventory constant. This was notably the case with PISCESv1 for CMIP5 (IPSL-CLM5A-LR/MR and IPSL-CM5B-LR) and with PISCESv2 for CMIP6 (IPSL-CM6A-LR). Although the balance of the global Alk inventory may be questioned at pre-industrial

states (Planchat et al., 2023), the use of an Alk restoration term may hide an imbalance in biogeochemical processes and may impact the carbon cycle. We therefore constrained the conservation of the global Alk inventory keeping a degree of freedom for the carbonate pump at the seafloor. Indeed, during the spin-up, at each time step, a coefficient is calculated at the global scale to adjust the fraction of PIC reaching the seafloor that is buried to counterbalance the net sink of Alk resulting from all the other biogeochemical processes affecting it (Fig. A1). After 2500 years of spin-up, we estimated the drift of this seafloor dissolution parameter low enough to fix it at the value obtained at the end of the spin-up. The strategy employed here – broadly similar to that developed in MARBL by NCAR (Long et al., 2021) and in COBALTv2 by NOAA-GFDL (Dunne et al., 2012) – only allows the global Alk inventory to be conserved relative to the biogeochemical processes that affect it. Surface dilution and concentration, as well as certain physical processes, which are not perfectly conservative in the model, lead to a slight negative Alk drift in the configuration used ($< 0.03\,\mathrm{Pg\,C\,yr^{-1}}$ in absolute terms), which is nevertheless of the same order of magnitude as the global net sink of the soft-tissue pump on Alk.

A3   RCP versus SSP

The use of the RCP8.5 scenario for the NEMO-PISCES sensitivity analysis is considered as a proof of concept, being slightly less extreme than the SSP5-8.5 scenario (Fig. A2).

Table A1. Summary of the CMIP6 ESMs, their coupled marine biogeochemical models and the experiments considered in this intercomparison.

Group	ESM	Marine biogeochemical model	Variant label	Experiments
CCCma	CanESM5	CMOC	r1i1p2f1	piControl, Historical, SSP1-2.6, SSP5-8.5
	CanESM5-CanOE	CanOE	r1i1p2f1	piControl, Historical, SSP1-2.6, SSP5-8.5
CMCC	CMCC-ESM2	BFM5.2	r1i1p1f1	piControl, Historical, SSP1-2.6, SSP5-8.5
CNRM-CERFACS	CNRM-ESM2-1	PISCESv2-gas	r1i1p1f2	piControl, Historical, SSP1-2.6, SSP5-8.5
CSIRO	ACCESS-ESM1-5	WOMBAT	r1i1p1f1	piControl, Historical, SSP1-2.6, SSP5-8.5
IPSL	IPSL-CM6A-LR	PISCESv2	r1i1p1f1	piControl, Historical, SSP1-2.6, SSP5-8.5
MIROC	MIROC-ES2L	OECO2	r1i1p1f2	piControl, Historical, SSP1-2.6, SSP5-8.5
MOHC	UKESM1-0-LL	MEDUSA-2.1	r1i1p1f2	piControl, Historical, SSP1-2.6, SSP5-8.5
MPI-M	MPI-ESM1-2-LR	HAMOCC6	r1i1p1f1	piControl, Historical, SSP1-2.6, SSP5-8.5
	MPI-ESM1-2-HR	HAMOCC6	r1i1p1f1	piControl, Historical, SSP1-2.6, SSP5-8.5
MRI	MRI-ESM2-0	NPZD-MRI	r1i2p1f1	piControl, Historical, SSP5-8.5
NCAR	CESM2-WACCM	MARBL	r1i1p1f1	piControl, Historical, SSP1-2.6, SSP5-8.5
NCC	NorESM2-LM	iHAMOCC	r1i1p1f1	piControl, Historical, SSP1-2.6, SSP5-8.5
NOAA-GFDL	GFDL-CM4	BLINGv2	r1i1p1f1	piControl, Historical, SSP5-8.5
	GFDL-ESM4	COBALTv2	r1i1p1f1	piControl, Historical, SSP1-2.6, SSP5-8.5

A4   NEMO-PISCES sensitivity simulations

Details regarding the sensitivity simulations carried out with NEMO-PISCES in this analysis are given in Table A2.

A5   Surface sAlk drifts

The surface sAlk faces a non-negligible drift for two ESMs in the CMIP6 ensemble: CMCC-ESM2 and CNRM-ESM2-1 (Fig. A3a). While this drift is directly associated with a surface Alk drift for CNRM-ESM2-1 (Fig. A3b), it is linked to a salinity drift in the case of CMCC-ESM2 (Fig. A3d), also impacting sDIC as a consequence (Fig. A3c).
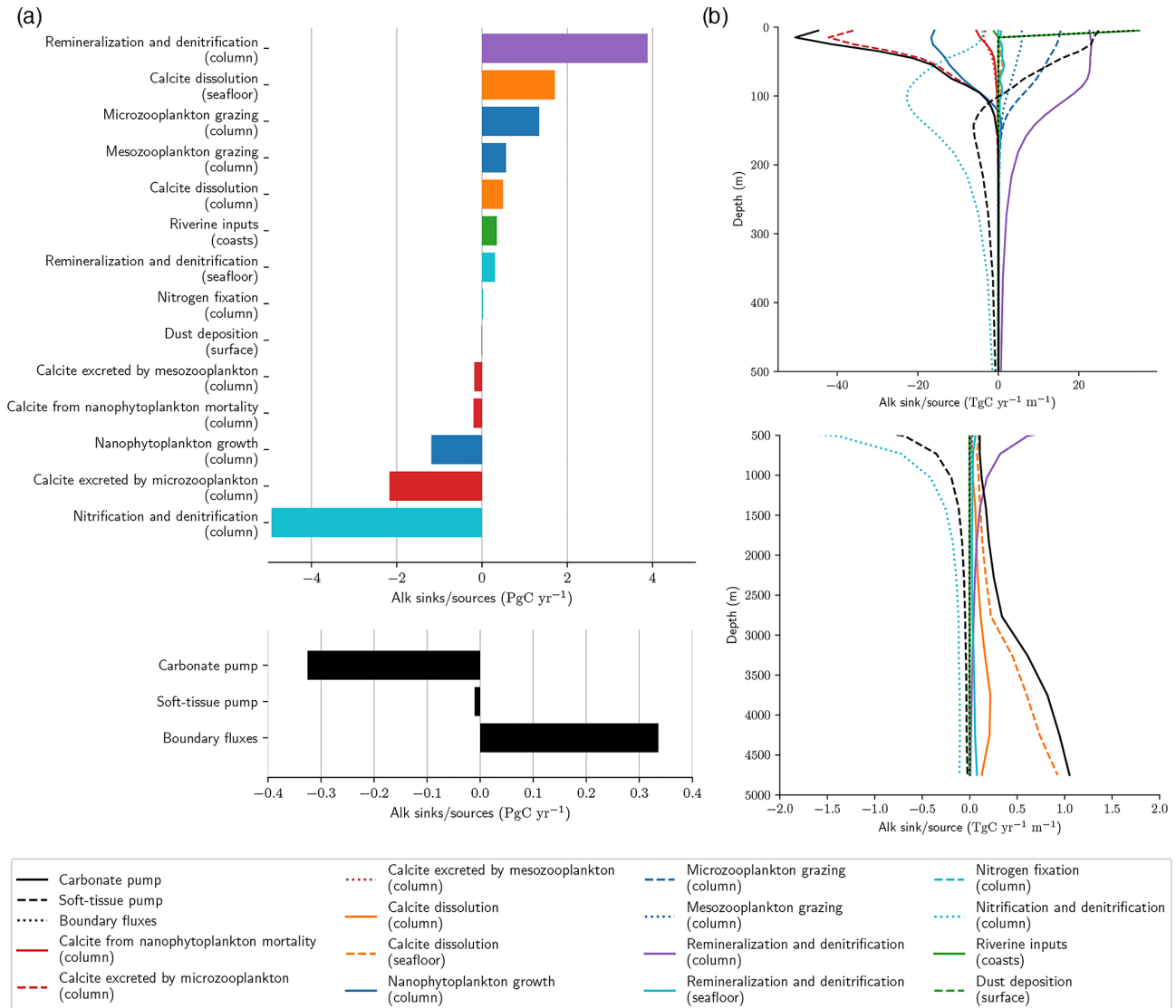
Figure A1. Alk sinks and sources in NEMO-PISCES pre-industrial standard simulation. Panel **(a)** shows integrated Alk sinks (negative) and sources (positive) associated with all the biogeochemical processes affecting it, which can occur in the water column, at the seafloor or the surface, or along the coasts. The colours refer to the type of processes affecting Alk associated with the following: (i) the carbonate pump through calcite production (red) and dissolution (orange); (ii) the soft-tissue pump through organic matter production (blue), organic matter remineralization (purple) and nitrogen reactions (cyan); and (iii) the boundary fluxes through riverine inputs and dust deposition (green). The net Alk budget for these three different components is shared in the bottom subpanel. Panel **(b)** shows vertical distribution of the global-scale area-weighted average of the various Alk sinks and sources, with a zoom on the first 500 m in the top subpanel.
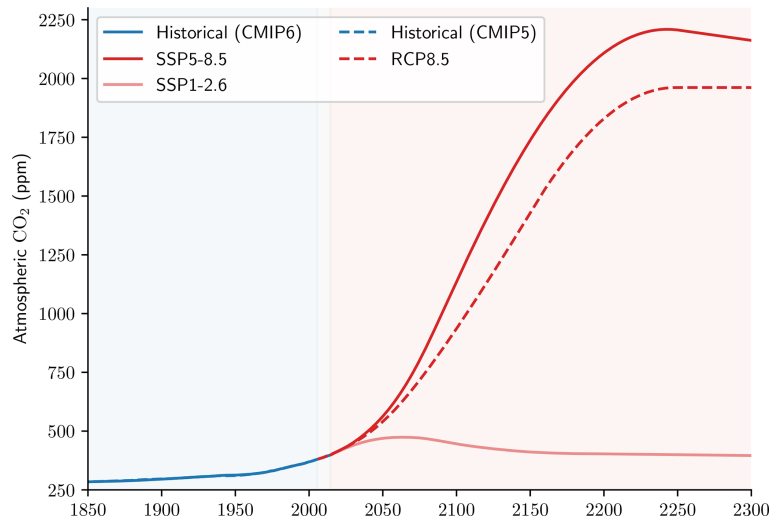
Figure A2. RCP versus SSP. Evolution of the atmospheric CO_2 concentration according to the scenarios considered in our analysis: (i) Historical (CMIP6), SSP5-8.5 and SSP1-2.6 for the CMIP6 ensemble; and (ii) Historical (CMIP5) and RCP8.5 for the NEMO-PISCES sensitivity simulations.

Table A2. Summary of the sensitivity simulations led with NEMO-PISCES. The key elements of these simulations, especially the forcing and parameters used, are shared for each of the experiments. Bold font highlights the simulations that are considered in the main text (e.g. Fig. 2), whereas simulations presented in roman font are only shown in Appendix (see Fig. B4) or for construction (e.g. the spin-up).

Simulation	Period	Atmospheric CO_2	Ocean dynamics	Production ratio parameter	Coefficient for the dissolved fraction at the seafloor
standard_spinup	1800–2299 (2500 years)	Pre-industrial	Pre-industrial	0.45	Free
standard_picontrol	1800–2299 (500 years)	Pre-industrial	Pre-industrial	0.45	0.934
standard	**1852–2299 (448 years)**	**Historical + RCP8.5**	**Pre-industrial**	**0.45**	**0.934**
carb–	**1852–2299 (448 years)**	**Historical + RCP8.5**	**Pre-industrial**	**0.45; decreased with atmospheric CO_2**	**0.934**
carb+	**1852–2299 (448 years)**	**Historical + RCP8.5**	**Pre-industrial**	**0.45; increased with atmospheric CO_2**	**0.934**
standard_dyn	1852–2299 (448 years)	Pre-industrial	Historical + RCP8.5	0.45	0.934
standard_dyn+atm	1852–2299 (448 years)	Historical + RCP8.5	Historical + RCP8.5	0.45	0.934
carb_low_spinup	1800–2299 (2500 years)	Pre-industrial	Pre-industrial	0.30	Free
carb_low_picontrol	1800–2299 (500 years)	Pre-industrial	Pre-industrial	0.30	0.789
carb_low	**1852–2299 (448 years)**	**Historical + RCP8.5**	**Pre-industrial**	**0.30**	**0.789**
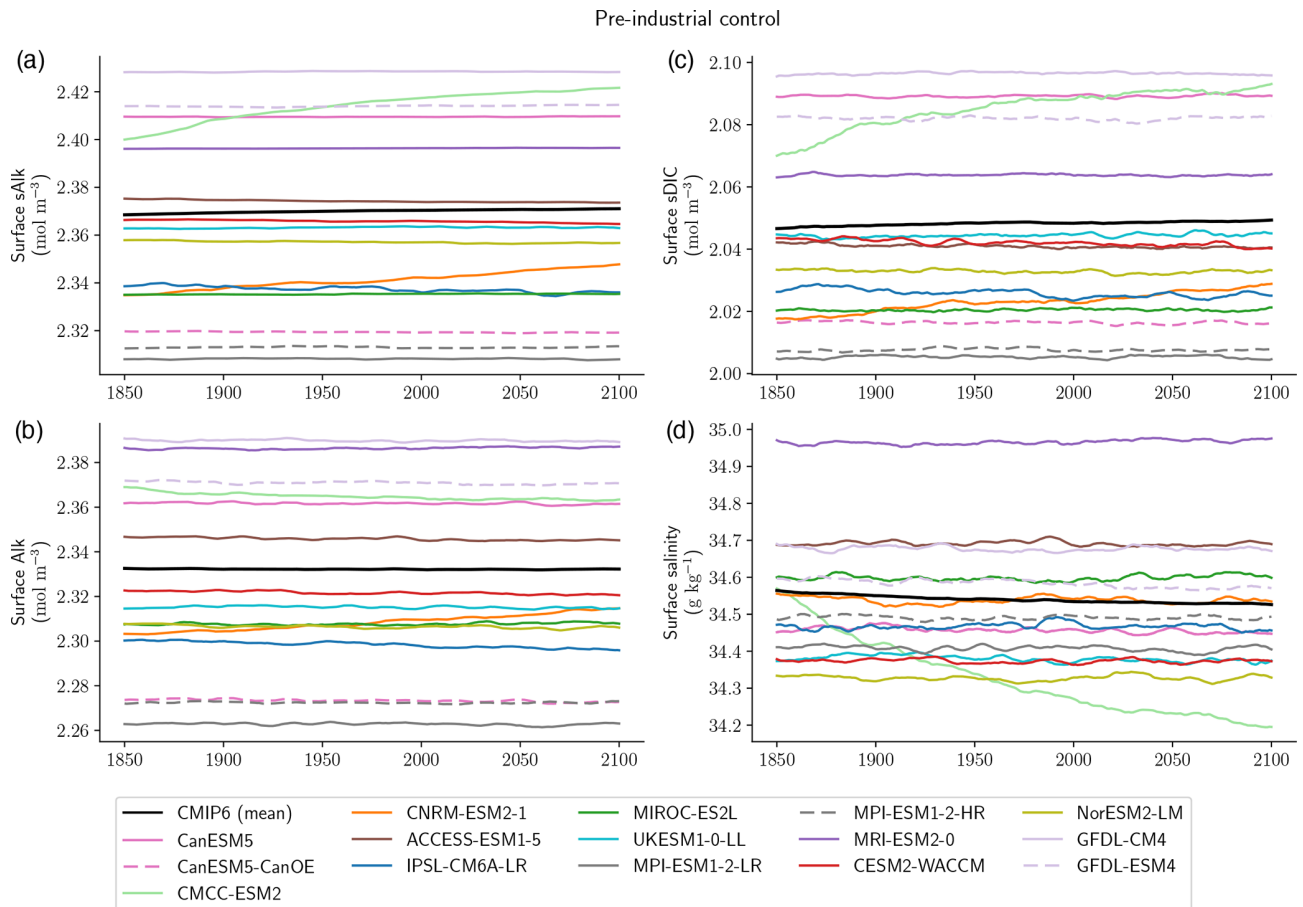
Figure A3. Surface sAlk drift, causes and consequences. Time series of the piControl experiment **(a)** surface sAlk, **(b)** surface Alk, **(c)** surface sDIC and **(d)** surface salinity for all the CMIP6 ensemble, as well as the ensemble mean.

Appendix B: Results and discussion

B1 Surface sAlk anomaly for 2081–2100

We share here a theoretical decomposition of the surface sAlk anomaly for 2081–2100 for the CMIP6 ensemble from the PIC and POC export anomalies at 100 m. To perform this decomposition, we use the relationship between the PIC export anomaly at 100 m and the surface sAlk anomaly that we obtained with the NEMO-PISCES sensitivity simulations. We use the slope of this linear regression $(-5.12 \times 10^{-2} \, \text{mol m}^{-3} \, (\text{PgC yr}^{-1})^{-1})$ to construct an indicative first-order transformation of the impact of a carbon particle export anomaly at 100 m on surface sDIC; a sort of conversion from petagrams of carbon per year to moles per cubic metre. We will note this parameter as c^0. Since Alk increases for a decrease in PIC export and is twice as impacted by a change in PIC export compared with DIC, $c^0 = -1 \times 0.5 \times (-5.12 \times 10^{-2}) = 2.06 \times 10^{-2} \, \text{mol m}^{-3} \, (\text{PgC yr}^{-1})^{-1}$. Then, the surface sAlk anomaly resulting from a PIC export anomaly at 100 m can be expressed as

$$\Delta sAlk_{\text{PIC}} = -\frac{2}{1} \cdot c_0 \cdot \Delta Ex(\text{PIC})^{100\,\text{m}}. \tag{B1}$$

Similarly, the surface sAlk anomaly relative to a POC export anomaly at 100 m can be expressed as

$$\Delta sAlk_{\text{POC}} = -\frac{-r_{\text{N:P}}}{r_{\text{C:P}}} \cdot c_0 \cdot \Delta Ex(\text{POC})^{100\,\text{m}}, \tag{B2}$$

where we consider that POC export anomalies induce surface anomalies with an ESM-dependent ratio equal to $-r_{\text{N:P}} : r_{\text{C:P}}$ (the opposite of the nitrogen to phosphorus ratio divided by the carbon to phosphorus ratio; see Planchat et al., 2023, their Supplement Table S1 for the associated values per ESM). In particular, the sAlk anomaly associated with POC is null for UKESM1-0-LL, since the soft-tissue pump does not affect Alk in MEDUSA-2.1 (see Planchat et al., 2023, their Supplement Table S1). Thus, as a first approximation, we can write a theoretical decomposition of the surface sAlk anomaly as

$$\Delta sAlk \approx \Delta sAlk_{\text{PIC}} + \Delta sAlk_{\text{POC}}. \tag{B3}$$

This decomposition is idealized. First, we consider that changes in the export at 100 m reflect surface sAlk changes. Second, the way we consider the effect of the POC export anomaly on sAlk is simplified, not taking into account the potential decoupling between the remineralization and the nitrogen reactions. Third, it does not take into account the consequences of the envisaged slowing of the meridional overturning circulation (MOC), which could have an impact on the surface sAlk (e.g. through an attenuation of the upwelling of Alk-enriched deep waters; Chikamoto et al., 2023). Nevertheless, it highlights the primary role of the PIC export anomaly in driving the surface sAlk anomaly by 2100 (Fig. B1a), with the POC export anomaly influence being second order (Fig. B1b). The combination of these two anomaly sources gives a result that is consistent with the modelled anomaly values in the CMIP6 ensemble for 2081–2100 (Fig. B1c). The fit can be further improved by increasing c_0, which is realistic, as climate change induces reduced ventilation, and thus a relative stagnation of surface waters, contrary to the idealized offline simulations we carried out with NEMO-PISCES, where only the concentration of atmospheric CO_2 varied. However, two models can be singled out: while CNRM-ESM2-1 stands out from the others due to its surface Alk drift (see Fig. A3a), CESM2-WACCM certainly stands out due to its slow circulation bias (Frischknecht et al., 2022), which would tend to accentuate the impact of a carbon export anomaly on the surface sAlk.

B2 Temporal and spatial trends

Additional information regarding PIC and POC export trends in the CMIP6 ensemble is presented in Figs. B2 and B3.

B3 Sensitivity simulations post-2100

We share here the extended time series and the full set of sensitivity simulations completed with NEMO-PISCES for the key variables considered in this analysis.
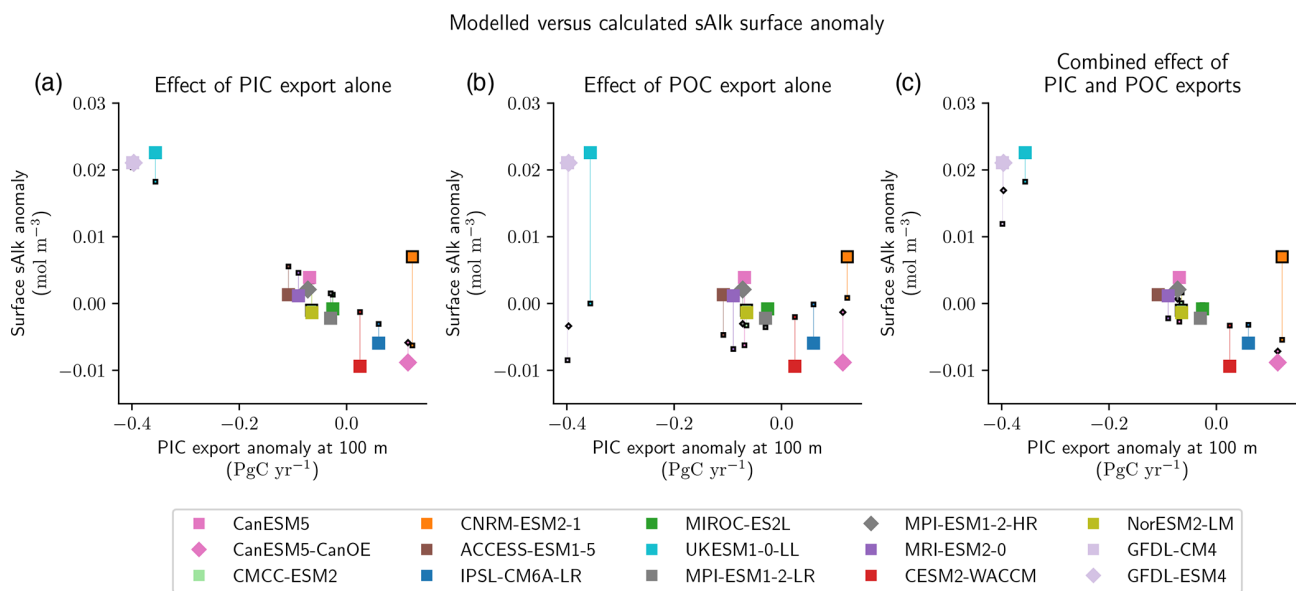
Figure B1. Theoretical decomposition of the sAlk surface anomaly, as a function of PIC export anomaly for all ESMs. Respective effect of the PIC **(a)** and POC **(b)** export anomalies at 100 m on the surface sAlk anomaly for 2081–2100. The combined effect of both export anomalies is displayed in **(c)**. For each of the three panels, in addition to the modelled values (big coloured squares and diamonds), the associated calculated values are displayed with small black-bordered symbols and linked by coloured lines. CMCC-ESM2 and CNRM-ESM2-1 are shown with a black-bordered symbol due to their surface sAlk drift (see Sect. 2.3 and Appendix B1).
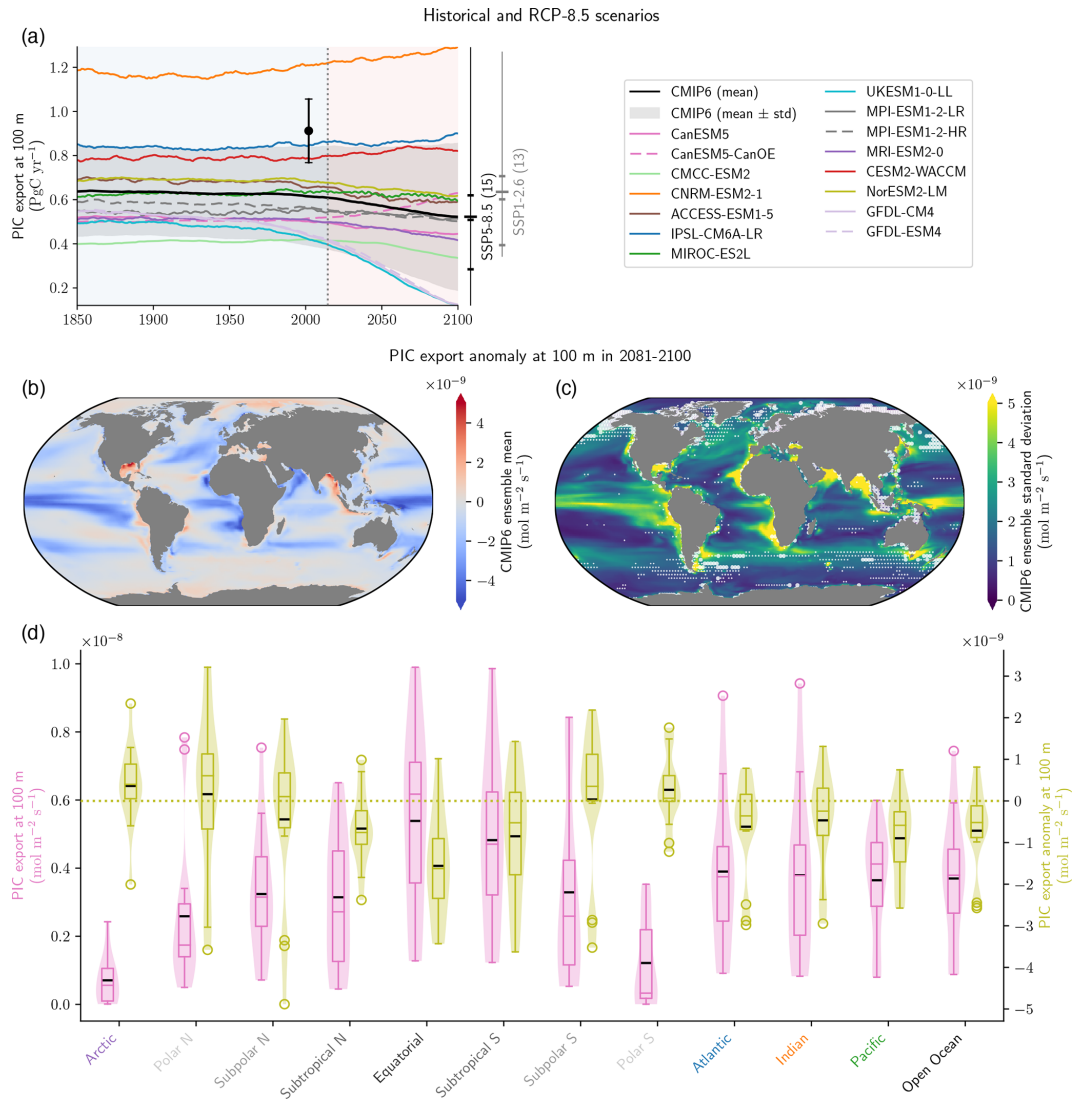
Figure B2. PIC export trends in the CMIP6 ensemble (supplement to Fig. 1a). Panel **(a)** shows the absolute values of PIC export at 100 m for the Historical and SSP5-8.5 experiments. The black dot refers to the observationally based estimate from Sulpis et al. (2021) – although referenced to 300 m – with its associated uncertainty. The data are smoothed with 11-year rolling means, and the number of ESMs available, means, quartiles and extreme values for 2100, for both SSP5-8.5 and SSP1-2.6, are provided. Panels **(b)** and **(c)** show the PIC export anomaly at 100 m for 2081–2100 relative to the pre-industrial state for **(b)** the CMIP6 ensemble mean and **(c)** the CMIP6 standard deviation. In **(c)**, partly transparent white circles point towards regions where strictly less than five ESMs (big circles) or strictly less than seven ESMs (small circles) agree on the sign of change with the CMIP6 ensemble mean. This white shading highlights areas where a few ESMs might strongly affect the CMIP6 ensemble mean value. Panel **(d)** is a violin plot of the PIC export at 100 m distribution at the pre-industrial state (pink) and for its anomaly for 2081–2100 (green) for specific open ocean basins (see Planchat et al., 2023, their Fig. A1).
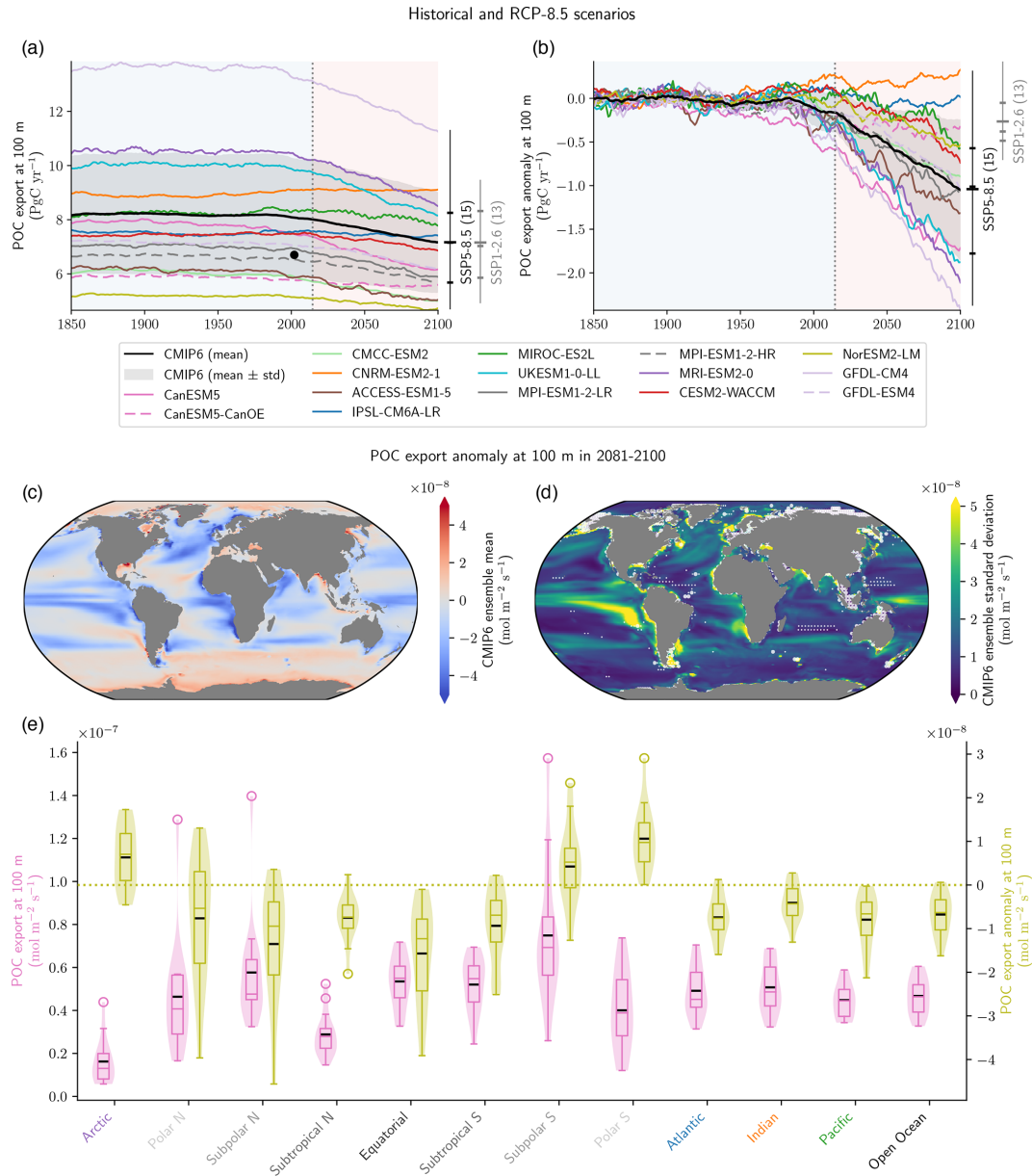
Figure B3. POC export trends in the CMIP6 ensemble (as for PIC export in Figs. B2 and 1a). Panel **(a)** shows the absolute values of POC export at 100 m for the Historical and SSP5-8.5 experiments. The black dot refers to the observationally based estimate from DeVries and Weber (2017). Panel **(b)** shows ESM projected anomalies relative to the pre-industrial control simulation in POC export at 100 m in the Historical and SSP5-8.5 simulations. In panels **(a)** and **(b)**, the data are smoothed with 11-year rolling means, and the number of ESMs available, means, quartiles and extreme values for 2100, for both SSP5-8.5 and SSP1-2.6, are provided. Panels **(c)** and **(d)** show the POC export anomaly at 100 m for 2081–2100 relative to the pre-industrial state for **(c)** the CMIP6 ensemble mean and **(d)** the CMIP6 standard deviation. In **(d)**, partly transparent white circles point towards regions where strictly less than five ESMs (big circles) or strictly less than seven ESMs (small circles) agree on the sign of change with the CMIP6 ensemble mean. This white shading highlights areas where a few ESMs might strongly affect the CMIP6 ensemble mean value. Panel **(e)** is a violin plot of the POC export at 100 m distribution at the pre-industrial state (pink) and for its anomaly for 2081–2100 (green) for specific open ocean basins (see Planchat et al., 2023, their Fig. A1).
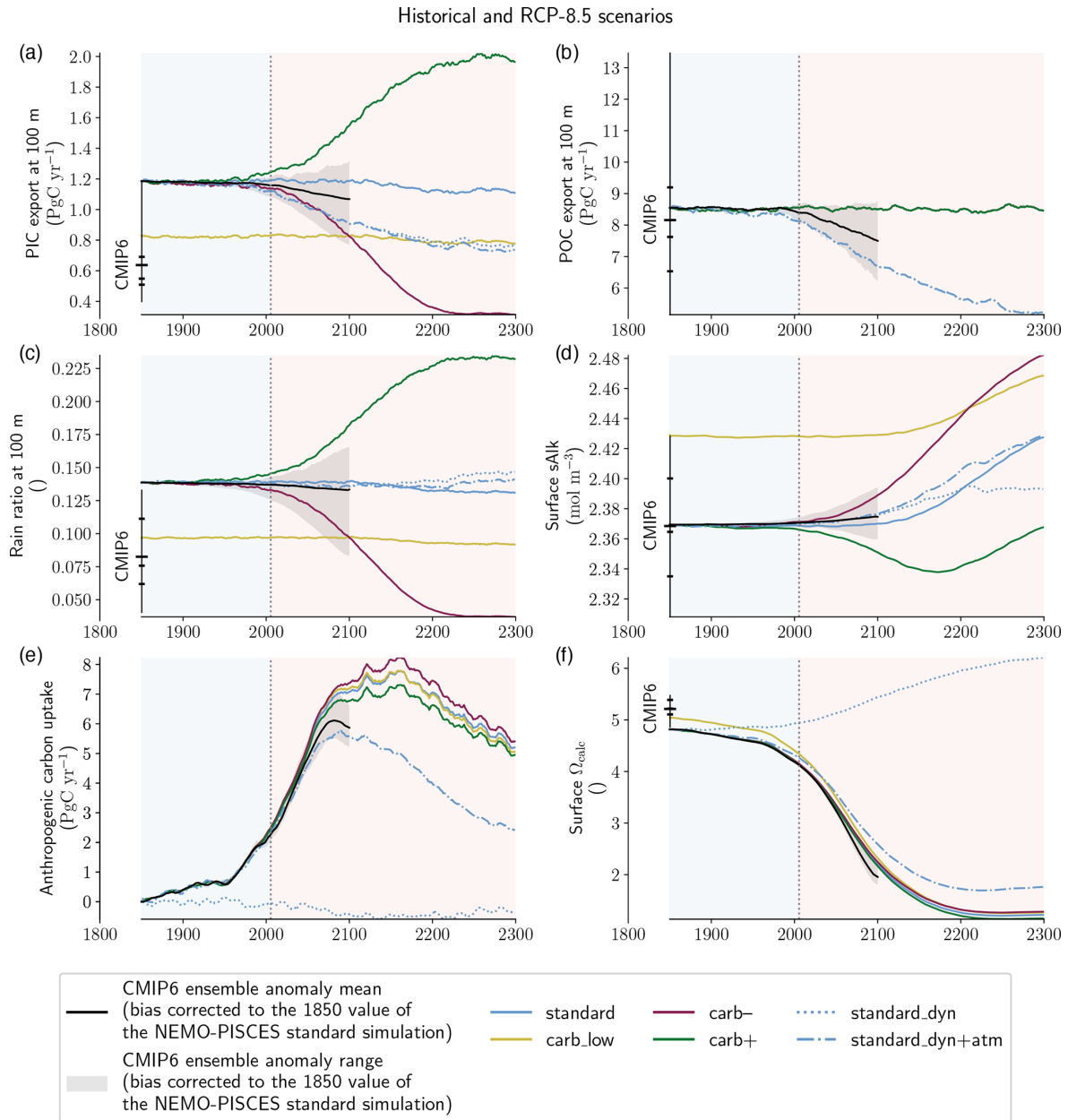
Figure B4. Sensitivity simulations with NEMO-PISCES (full time series and full set of NEMO-PISCES simulations; see Table A2). Absolute values of **(a)** PIC export at 100 m, **(b)** POC export at 100 m, **(c)** the rain ratio at 100 m, **(d)** surface sAlk, **(e)** anthropogenic carbon uptake and **(f)** surface calcite saturation state for all the sensitivity simulations. For each panel, the data are smoothed with 11-year rolling means, and CMIP6 ensemble statistical elements (mean, quartiles and extreme values) are provided for early Historical experiment values for 1850. The CMIP6 ensemble anomaly mean (black line) and range (grey shading) are shown bias corrected to the 1850 value of the NEMO-PISCES standard simulation.

Author contributions. This work is in the framework of the OMIP-BGC group, which contributed collectively to this study through the organization and execution of the CMIP exercises and the sharing of simulation outputs. AP: conceptualization, investigation, methodology, formal analysis, visualization, writing – original draft preparation – and project administration. LB and LK: supervision, funding acquisition, methodology, resources, conceptualization and writing – original draft preparation. OT: software.

References

Arora, V. K., Katavouta, A., Williams, R. G., Jones, C. D., Brovkin, V., Friedlingstein, P., Schwinger, J., Bopp, L., Boucher, O., Cadule, P., Chamberlain, M. A., Christian, J. R., Delire, C., Fisher, R. A., Hajima, T., Ilyina, T., Joetzjer, E., Kawamiya, M., Koven, C. D., Krasting, J. P., Law, R. M., Lawrence, D. M., Lenton, A., Lindsay, K., Pongratz, J., Raddatz, T., Séférian, R., Tachiiri, K., Tjiputra, J. F., Wiltshire, A., Wu, T., and Ziehn, T.: Carbon–concentration and carbon–climate feedbacks in CMIP6 models and their comparison to CMIP5 models, Biogeosciences, 17, 4173–4222, https://doi.org/10.5194/bg-17-4173-2020, 2020.

Aumont, O., Ethé, C., Tagliabue, A., Bopp, L., and Gehlen, M.: PISCES-v2: an ocean biogeochemical model for carbon and ecosystem studies, Geosci. Model Dev., 8, 2465–2513, https://doi.org/10.5194/gmd-8-2465-2015, 2015.

Bindoff, N., Cheung, W., Kairo, J., Arístegui, J., Guinder, V., Hallberg, R., Hilmi, N., Jiao, N., Karim, M., Levin, L., O'Donoghue, S., Cuicapusa, S., Rinkevich, B., Suga, T., Tagliabue, A., and Williamson, P.: Changing Ocean, Marine Ecosystems, and Dependent Communities, in: Special Report on the Ocean and Cryosphere in a Changing Climate, Cambridge University Press, 447–587, https://doi.org/10.1017/9781009157964.007, 2019.

Bopp, L., Resplandy, L., Orr, J. C., Doney, S. C., Dunne, J. P., Gehlen, M., Halloran, P., Heinze, C., Ilyina, T., Séférian, R., Tjiputra, J., and Vichi, M.: Multiple stressors of ocean ecosystems in the 21st century: projections with CMIP5 models, Biogeosciences, 10, 6225–6245, https://doi.org/10.5194/bg-10-6225-2013, 2013.

Bopp, L., Aumont, O., Kwiatkowski, L., Clerc, C., Dupont, L., Ethé, C., Gorgues, T., Séférian, R., and Tagliabue, A.: Diazotrophy as a key driver of the response of marine net primary productivity to climate change, Biogeosciences, 19, 4267–4285, https://doi.org/10.5194/bg-19-4267-2022, 2022.

Boudreau, B. P., Middelburg, J. J., and Luo, Y.: The role of calcification in carbonate compensation, Nat. Geosci., 11, 894–900, https://doi.org/10.1038/s41561-018-0259-5, 2018.

Broecker, W. S. and Peng, T.-H.: The role of $CaCO_3$ compensation in the glacial to interglacial atmospheric CO_2 change, Global Biogeochem. Cy., 1, 15–29, https://doi.org/10.1029/GB001i001p00015, 1987.

Canadell, J., Monteiro, P., Costa, M., Cotrim da Cunha, L., Cox, P., Eliseev, A., Henson, S., Ishii, M., Jaccard, S., Koven, C., Lohila, A., Patra, P., Piao, S., Rogelj, J., Syampungani, S., Zaehle, S., and Zickfeld, K.: Global Carbon and other Biogeochemical Cycles and Feedbacks, in: Climate Change 2021: The Physical Science Basis. Contribution of Working Group I to the Sixth Assessment Report of the Intergovernmental Panel on Climate Change,

edited by: Masson-Delmotte, V., Zhai, P., Pirani, A., Connors, S., Péan, C., Berger, S., Caud, N., Chen, Y., Goldfarb, L., Gomis, M., Huang, M., Leitzell, K., Lonnoy, E., Matthews, J., Maycock, T., Waterfield, T., Yelekçi, O., Yu, R., and Zhou, B., Cambridge University Press, Cambridge, United Kingdom and New York, NY, USA, https://doi.org/10.1017/9781009157896.007, pp. 673–816, 2021.

Carter, B. R., Frölicher, T. L., Dunne, J. P., Rodgers, K. B., Slater, R. D., and Sarmiento, J. L.: When can ocean acidification impacts be detected from decadal alkalinity measurements?, Global Biogeochem. Cy., 30, 595–612, https://doi.org/10.1002/2015GB005308, 2016.

Chen, D., Rojas, M., Samset, B., Cobb, K., Niang, A., Edwards, P., Emori, S., Faria, S., Hawkins, E., Hope, P., Huybrechts, P., Meinshausen, M., Mustafa, S., Plattner, G.-K., Tréguier, A.-M., V., P., Pirani, A., Connors, S., Péan, C., Berger, S., Caud, N., Chen, Y., Goldfarb, L., Gomis, M., Huang, M., Leitzell, K., and Lonnoy, E.: Framing, Context, and Methods, in: Climate Change 2021: The Physical Science Basis. Contribution of Working Group I to the Sixth Assessment Report of the Intergovernmental Panel on Climate Change, Cambridge University Press, 147–286, https://doi.org/10.1017/9781009157896.003, 2021.

Chikamoto, M. O., DiNezio, P., and Lovenduski, N.: Long-Term Slowdown of Ocean Carbon Uptake by Alkalinity Dynamics, Geophys. Res. Lett., 50, e2022GL101954, https://doi.org/10.1029/2022GL101954, 2023.

Crutzen, P. J. and Stoermer, E. F.: Global change newsletter, Anthropocene, 41, 17–18, 2000.

De La Rocha, C. L. and Passow, U.: Factors influencing the sinking of POC and the efficiency of the biological carbon pump, Deep-Sea Res. Pt. II, 54, 639–658, https://doi.org/10.1016/j.dsr2.2007.01.004, 2007.

DeVries, T. and Weber, T.: The export and fate of organic matter in the ocean: New constraints from combining satellite and oceanographic tracer observations, Global Biogeochem. Cy., 31, 535–555, https://doi.org/10.1002/2016GB005551, 2017.

Dickson, A. G., Sabine, C. L., Christian, J. R., Bargeron, C. P., and Organization, N. P. M. S., eds.: Guide to best practices for ocean CO_2 measurements, no. 3 in PICES special publication, North Pacific Marine Science Organization, Sidney, BC, 2007.

Dufresne, J.-L., Foujols, M.-A., Denvil, S., Caubel, A., Marti, O., Aumont, O., Balkanski, Y., Bekki, S., Bellenger, H., Benshila, R., Bony, S., Bopp, L., Braconnot, P., Brockmann, P., Cadule, P., Cheruy, F., Codron, F., Cozic, A., Cugnet, D., de Noblet, N., Duvel, J.-P., Ethé, C., Fairhead, L., Fichefet, T., Flavoni, S., Friedlingstein, P., Grandpeix, J.-Y., Guez, L., Guilyardi, E., Hauglustaine, D., Hourdin, F., Idelkadi, A., Ghattas, J., Joussaume, S., Kageyama, M., Krinner, G., Labetoulle, S., Lahellec, A., Lefebvre, M.-P., Lefevre, F., Levy, C., Li, Z. X., Lloyd, J., Lott, F., Madec, G., Mancip, M., Marchand, M., Masson, S., Meurdesoif, Y., Mignot, J., Musat, I., Parouty, S., Polcher, J., Rio, C., Schulz, M., Swingedouw, D., Szopa, S., Talandier, C., Terray, P., Viovy, N., and Vuichard, N.: Climate change projections using the IPSL-CM5 Earth System Model: from CMIP3 to CMIP5, Clim. Dynam., 40, 2123–2165, https://doi.org/10.1007/s00382-012-1636-1, 2013.

Dunne, J. P., Hales, B., and Toggweiler, J. R.: Global calcite cycling constrained by sediment preservation con-

trols, Global Biogeochem. Cy., 26, 2010GB003935, https://doi.org/10.1029/2010GB003935, 2012.

Engel, A., Szlosek, J., Abramson, L., Liu, Z., and Lee, C.: Investigating the effect of ballasting by $CaCO_3$ in Emiliania huxleyi: I. Formation, settling velocities and physical properties of aggregates, Deep-Sea Res. Pt. II, 56, 1396–1407, https://doi.org/10.1016/j.dsr2.2008.11.027, 2009.

ESGF: ESGF node at IPSL, https://esgf-node.ipsl.upmc.fr/projects/esgf-ipsl/, last access: June 2023.

Eyring, V., Bony, S., Meehl, G. A., Senior, C. A., Stevens, B., Stouffer, R. J., and Taylor, K. E.: Overview of the Coupled Model Intercomparison Project Phase 6 (CMIP6) experimental design and organization, Geosci. Model Dev., 9, 1937–1958, https://doi.org/10.5194/gmd-9-1937-2016, 2016.

Friedlingstein, P., O'Sullivan, M., Jones, M. W., Andrew, R. M., Gregor, L., Hauck, J., Le Quéré, C., Luijkx, I. T., Olsen, A., Peters, G. P., Peters, W., Pongratz, J., Schwingshackl, C., Sitch, S., Canadell, J. G., Ciais, P., Jackson, R. B., Alin, S. R., Alkama, R., Arneth, A., Arora, V. K., Bates, N. R., Becker, M., Bellouin, N., Bittig, H. C., Bopp, L., Chevallier, F., Chini, L. P., Cronin, M., Evans, W., Falk, S., Feely, R. A., Gasser, T., Gehlen, M., Gkritzalis, T., Gloege, L., Grassi, G., Gruber, N., Gürses, Ö., Harris, I., Hefner, M., Houghton, R. A., Hurtt, G. C., Iida, Y., Ilyina, T., Jain, A. K., Jersild, A., Kadono, K., Kato, E., Kennedy, D., Klein Goldewijk, K., Knauer, J., Korsbakken, J. I., Landschützer, P., Lefèvre, N., Lindsay, K., Liu, J., Liu, Z., Marland, G., Mayot, N., McGrath, M. J., Metzl, N., Monacci, N. M., Munro, D. R., Nakaoka, S.-I., Niwa, Y., O'Brien, K., Ono, T., Palmer, P. I., Pan, N., Pierrot, D., Pocock, K., Poulter, B., Resplandy, L., Robertson, E., Rödenbeck, C., Rodriguez, C., Rosan, T. M., Schwinger, J., Séférian, R., Shutler, J. D., Skjelvan, I., Steinhoff, T., Sun, Q., Sutton, A. J., Sweeney, C., Takao, S., Tanhua, T., Tans, P. P., Tian, X., Tian, H., Tilbrook, B., Tsujino, H., Tubiello, F., van der Werf, G. R., Walker, A. P., Wanninkhof, R., Whitehead, C., Willstrand Wranne, A., Wright, R., Yuan, W., Yue, C., Yue, X., Zaehle, S., Zeng, J., and Zheng, B.: Global Carbon Budget 2022, Earth Syst. Sci. Data, 14, 4811–4900, https://doi.org/10.5194/essd-14-4811-2022, 2022.

Friis, K., Körtzinger, A., and Wallace, D. W. R.: The salinity normalization of marine inorganic carbon chemistry data, Geophys. Res. Lett., 30, 1085, https://doi.org/10.1029/2002GL015898, 2003.

Frischknecht, T., Ekici, A., and Joos, F.: Radiocarbon in the Land and Ocean Components of the Community Earth System Model, Global Biogeochem. Cy., 36, e2021GB007042, https://doi.org/10.1029/2021GB007042, 2022.

Fry, C. H., Tyrrell, T., Hain, M. P., Bates, N. R., and Achterberg, E. P.: Analysis of global surface ocean alkalinity to determine controlling processes, Mar. Chem., 174, 46–57, https://doi.org/10.1016/j.marchem.2015.05.003, 2015.

Fu, W., Randerson, J. T., and Moore, J. K.: Climate change impacts on net primary production (NPP) and export production (EP) regulated by increasing stratification and phytoplankton community structure in the CMIP5 models, Biogeosciences, 13, 5151–5170, https://doi.org/10.5194/bg-13-5151-2016, 2016.

Gangstø, R., Joos, F., and Gehlen, M.: Sensitivity of pelagic calcification to ocean acidification, Biogeosciences, 8, 433–458, https://doi.org/10.5194/bg-8-433-2011, 2011.

Gattuso, J.-P. and Hansson, L. (Eds.): Ocean acidification, Oxford University Press, Oxford, New York, oCLC: ocn730413873, ISBN: 9780199591091, 2011.

Gehlen, M., Gangstø, R., Schneider, B., Bopp, L., Aumont, O., and Ethe, C.: The fate of pelagic $CaCO_3$ production in a high CO_2 ocean: a model study, Biogeosciences, 4, 505–519, https://doi.org/10.5194/bg-4-505-2007, 2007.

Hain, M. P., Sigman, D. M., and Haug, G. H.: Elemental and Isotopic Proxies of Past Ocean Temperatures, in: Treatise on Geochemistry, Elsevier, https://doi.org/10.1016/B978-0-08-095975-7.00614-8, pp. 373–397, 2014.

Henson, S. A., Laufkötter, C., Leung, S., Giering, S. L. C., Palevsky, H. I., and Cavan, E. L.: Uncertain response of ocean biological carbon export in a changing world, Nat. Geosci., 15, 248–254, https://doi.org/10.1038/s41561-022-00927-0, 2022.

Hofmann, M. and Schellnhuber, H.-J.: Oceanic acidification affects marine carbon pump and triggers extended marine oxygen holes, P. Natl. Acad. Sci. USA, 106, 3017–3022, https://doi.org/10.1073/pnas.0813384106, 2009.

Ilyina, T., Zeebe, R. E., Maier-Reimer, E., and Heinze, C.: Early detection of ocean acidification effects on marine calcification, Global Biogeochem. Cy., 23, GB1008, https://doi.org/10.1029/2008GB003278, 2009.

Klaas, C. and Archer, D. E.: Association of sinking organic matter with various types of mineral ballast in the deep sea: Implications for the rain ratio, Global Biogeochem. Cy., 16, 63–1–63–14, https://doi.org/10.1029/2001GB001765, 2002.

Kroeker, K. J., Kordas, R. L., Crim, R., Hendriks, I. E., Ramajo, L., Singh, G. S., Duarte, C. M., and Gattuso, J.-P.: Impacts of ocean acidification on marine organisms: quantifying sensitivities and interaction with warming, Glob. Change Biol., 19, 1884–1896, https://doi.org/10.1111/gcb.12179, 2013.

Krumhardt, K. M., Lovenduski, N. S., Long, M. C., Levy, M., Lindsay, K., Moore, J. K., and Nissen, C.: Coccolithophore Growth and Calcification in an Acidified Ocean: Insights From Community Earth System Model Simulations, J. Adv. Model. Earth Sy., 11, 1418–1437, https://doi.org/10.1029/2018MS001483, 2019.

Kurahashi-Nakamura, T., Paul, A., Merkel, U., and Schulz, M.: Glacial state of the global carbon cycle: time-slice simulations for the last glacial maximum with an Earth-system model, Clim. Past, 18, 1997–2019, https://doi.org/10.5194/cp-18-1997-2022, 2022.

Kwiatkowski, L., Torres, O., Bopp, L., Aumont, O., Chamberlain, M., Christian, J. R., Dunne, J. P., Gehlen, M., Ilyina, T., John, J. G., Lenton, A., Li, H., Lovenduski, N. S., Orr, J. C., Palmieri, J., Santana-Falcón, Y., Schwinger, J., Séférian, R., Stock, C. A., Tagliabue, A., Takano, Y., Tjiputra, J., Toyama, K., Tsujino, H., Watanabe, M., Yamamoto, A., Yool, A., and Ziehn, T.: Twenty-first century ocean warming, acidification, deoxygenation, and upper-ocean nutrient and primary production decline from CMIP6 model projections, Biogeosciences, 17, 3439–3470, https://doi.org/10.5194/bg-17-3439-2020, 2020.

Laufkötter, C., Vogt, M., Gruber, N., Aita-Noguchi, M., Aumont, O., Bopp, L., Buitenhuis, E., Doney, S. C., Dunne, J., Hashioka, T., Hauck, J., Hirata, T., John, J., Le Quéré, C., Lima, I. D., Nakano, H., Seferian, R., Totterdell, I., Vichi, M., and Völker, C.: Drivers and uncertainties of future global marine primary production in marine ecosystem models, Biogeosciences, 12, 6955–6984, https://doi.org/10.5194/bg-12-6955-2015, 2015.

Laufkötter, C., Vogt, M., Gruber, N., Aumont, O., Bopp, L., Doney, S. C., Dunne, J. P., Hauck, J., John, J. G., Lima, I. D., Seferian, R., and Völker, C.: Projected decreases in future marine export production: the role of the carbon flux through the upper ocean ecosystem, Biogeosciences, 13, 4023–4047, https://doi.org/10.5194/bg-13-4023-2016, 2016.

Lee, C., Peterson, M. L., Wakeham, S. G., Armstrong, R. A., Cochran, J. K., Miquel, J. C., Fowler, S. W., Hirschberg, D., Beck, A., and Xue, J.: Particulate organic matter and ballast fluxes measured using time-series and settling velocity sediment traps in the northwestern Mediterranean Sea, Deep-Sea Res. Pt. II, 56, 1420–1436, https://doi.org/10.1016/j.dsr2.2008.11.029, 2009.

Leung, J. Y. S., Zhang, S., and Connell, S. D.: Is Ocean Acidification Really a Threat to Marine Calcifiers? A Systematic Review and Meta-Analysis of 980+ Studies Spanning Two Decades, Small, 18, 2107407, https://doi.org/10.1002/smll.202107407, 2022.

Levin, L. A. and Le Bris, N.: The deep ocean under climate change, Science, 350, 766–768, https://doi.org/10.1126/science.aad0126, 2015.

Long, M. C., Moore, J. K., Lindsay, K., Levy, M. N., Doney, S. C., Luo, J. Y., Krumhardt, K. M., Letscher, R. T., Grover, M., and Sylvester, Z. T.: Simulations with the Marine Biogeochemistry Library (MARBL), J. Adv. Model. Earth Sy., 13, e2021MS002647, https://doi.org/10.1029/2021MS002647, 2021.

Meyer, J. and Riebesell, U.: Reviews and Syntheses: Responses of coccolithophores to ocean acidification: a meta-analysis, Biogeosciences, 12, 1671–1682, https://doi.org/10.5194/bg-12-1671-2015, 2015.

Moriceau, B., Goutx, M., Guigue, C., Lee, C., Armstrong, R., Duflos, M., Tamburini, C., Charrière, B., and Ragueneau, O.: Si–C interactions during degradation of the diatom Skeletonema marinoi, Deep-Sea Res. Pt. II, 56, 1381–1395, https://doi.org/10.1016/j.dsr2.2008.11.026, 2009.

Olsen, A., Lange, N., Key, R. M., Tanhua, T., Bittig, H. C., Kozyr, A., Álvarez, M., Azetsu-Scott, K., Becker, S., Brown, P. J., Carter, B. R., Cotrim da Cunha, L., Feely, R. A., van Heuven, S., Hoppema, M., Ishii, M., Jeansson, E., Jutterström, S., Landa, C. S., Lauvset, S. K., Michaelis, P., Murata, A., Pérez, F. F., Pfeil, B., Schirnick, C., Steinfeldt, R., Suzuki, T., Tilbrook, B., Velo, A., Wanninkhof, R., and Woosley, R. J.: An updated version of the global interior ocean biogeochemical data product, GLODAPv2.2020, Earth Syst. Sci. Data, 12, 3653–3678, https://doi.org/10.5194/essd-12-3653-2020, 2020.

Orr, J. C. and Epitalon, J.-M.: Improved routines to model the ocean carbonate system: mocsy 2.0, Geosci. Model Dev., 8, 485–499, https://doi.org/10.5194/gmd-8-485-2015, 2015.

Passow, U. and De La Rocha, C. L.: Accumulation of mineral ballast on organic aggregates, Global Biogeochem. Cy., 20, https://doi.org/10.1029/2005GB002579, 2006.

Pinsonneault, A. J., Matthews, H. D., Galbraith, E. D., and Schmittner, A.: Calcium carbonate production response to future ocean warming and acidification, Biogeosciences, 9, 2351–2364, https://doi.org/10.5194/bg-9-2351-2012, 2012.

Planchat, A.: Alkalinity and calcium carbonate in Earth system models, and implications for the ocean carbon cycle, Zenodo [code], https://doi.org/10.5281/zenodo.8421951, 2023.

Planchat, A., Kwiatkowski, L., Bopp, L., Torres, O., Christian, J. R., Butenschön, M., Lovato, T., Séférian, R., Chamberlain, M. A., Aumont, O., Watanabe, M., Yamamoto, A., Yool, A., Ilyina, T., Tsujino, H., Krumhardt, K. M., Schwinger, J., Tjiputra, J., Dunne, J. P., and Stock, C.: The representation of alkalinity and the carbonate pump from CMIP5 to CMIP6 Earth system models and implications for the carbon cycle, Biogeosciences, 20, 1195–1257, https://doi.org/10.5194/bg-20-1195-2023, 2023.

Revelle, R. and Suess, H. E.: Carbon Dioxide Exchange Between Atmosphere and Ocean and the Question of an Increase of Atmospheric CO_2 during the Past Decades, Tellus, 9, 18–27, https://doi.org/10.1111/j.2153-3490.1957.tb01849.x, 1957.

Ridgwell, A., Zondervan, I., Hargreaves, J. C., Bijma, J., and Lenton, T. M.: Assessing the potential long-term increase of oceanic fossil fuel CO_2 uptake due to CO_2−calcification feedback, Biogeosciences, 4, 481–492, https://doi.org/10.5194/bg-4-481-2007, 2007.

Ridgwell, A. J., Watson, A. J., Maslin, M. A., and Kaplan, J. O.: Implications of coral reef buildup for the controls on atmospheric CO_2 since the Last Glacial Maximum, Paleoceanography, 18, 1083, https://doi.org/10.1029/2003PA000893, 2003.

Sarmiento, J. L. and Gruber, N.: Ocean biogeochemical dynamics, Princeton University Press, Princeton, oCLC: ocm60651167, https://doi.org/10.1515/9781400849079, 2006.

Sarmiento, J. L., Hughes, T. M. C., Stouffer, R. J., and Manabe, S.: Simulated response of the ocean carbon cycle to anthropogenic climate warming, Nature, 393, 245–249, https://doi.org/10.1038/30455, 1998.

Schmittner, A., Oschlies, A., Matthews, H. D., and Galbraith, E. D.: Future changes in climate, ocean circulation, ecosystems, and biogeochemical cycling simulated for a business-as-usual CO_2 emission scenario until year 4000 AD, Global Biogeochem. Cy., 22, https://doi.org/10.1029/2007GB002953, 2008.

Schwinger, J., Tjiputra, J. F., Heinze, C., Bopp, L., Christian, J. R., Gehlen, M., Ilyina, T., Jones, C. D., Salas-Mélia, D., Segschneider, J., Séférian, R., and Totterdell, I.: Nonlinearity of Ocean Carbon Cycle Feedbacks in CMIP5 Earth System Models, J. Climate, 27, 3869–3888, https://doi.org/10.1175/JCLI-D-13-00452.1, 2014.

Seifert, M., Rost, B., Trimborn, S., and Hauck, J.: Meta-analysis of multiple driver effects on marine phytoplankton highlights modulating role of pCO_2, Glob. Change Biol., 26, 6787–6804, https://doi.org/10.1111/gcb.15341, 2020.

Seifert, M., Nissen, C., Rost, B., and Hauck, J.: Cascading effects augment the direct impact of CO_2 on phytoplankton growth in a biogeochemical model, Elementa: Science of the Anthropocene, 10, 00104, https://doi.org/10.1525/elementa.2021.00104, 2022.

Sigman, D. M. and Boyle, E. A.: Glacial/interglacial variations in atmospheric carbon dioxide, Nature, 407, 859–869, https://doi.org/10.1038/35038000, 2000.

Subhas, A. V., Rollins, N. E., Berelson, W. M., Dong, S., Erez, J., and Adkins, J. F.: A novel determination of calcite dissolution kinetics in seawater, Geochim. Cosmochim. Ac., 170, 51–68, https://doi.org/10.1016/j.gca.2015.08.011, 2015.

Sulpis, O., Jeansson, E., Dinauer, A., Lauvset, S. K., and Middelburg, J. J.: Calcium carbonate dissolution patterns in the ocean, Nat. Geosci., 14, 423–428, https://doi.org/10.1038/s41561-021-00743-y, 2021.

Tagliabue, A., Kwiatkowski, L., Bopp, L., Butenschön, M., Cheung, W., Lengaigne, M., and Vialard, J.: Persistent Uncertainties in Ocean Net Primary Production Climate Change Projections at Regional Scales Raise Challenges for Assessing Impacts on Ecosystem Services, Frontiers in Climate, 3, https://doi.org/10.3389/fclim.2021.738224, 2021.

Wilson, J. D., Andrews, O., Katavouta, A., de Melo Viríssimo, F., Death, R. M., Adloff, M., Baker, C. A., Blackledge, B., Goldsworth, F. W., Kennedy-Asser, A. T., Liu, Q., Sieradzan, K. R., Vosper, E., and Ying, R.: The biological carbon pump in CMIP6 models: 21st century trends and uncertainties, P. Natl. Acad. Sci. USA, 119, e2204369119, https://doi.org/10.1073/pnas.2204369119, 2022.

Zeebe, R. E. and Wolf-Gladrow, D.: CO_2 in seawater: equilibrium, kinetics, isotopes, Gulf Professional Publishing, Vol. 65, ISBN 9780444509468, 2001.

Zondervan, I., Zeebe, R. E., Rost, B., and Riebesell, U.: Decreasing marine biogenic calcification: A negative feedback on rising atmospheric pCO_2, Global Biogeochem. Cy., 15, 507–516, https://doi.org/10.1029/2000GB001321, 2001.